UNIVERSITÉ DU QUÉBEC À RIMOUSKI

ANALYSE ET MODÉLISATION DE LA PROPAGATION DU SPECTRE DE VAGUE DANS LES MERS ENGLACÉES

Thèse présentée

dans le cadre du programme de maîtrise en océanographie

en vue de l'obtention du grade de Maître ès sciences (M.Sc.)

PAR

©SÉBASTIEN DUGAS

Avril 2020

Composition du jury :

Daniel Bourgault, président du jury, Université du Québec à Rimouski

Cédric Chavanne, directeur de recherche, Université du Québec à Rimouski

Dany Dumont, codirecteur de recherche, Université du Québec à Rimouski

Graig Sutherland, examinateur externe, Environnement Canada

Dépôt initial le 10 avril 2020 Dépôt final le 11 août 2020

UNIVERSITÉ DU QUÉBEC À RIMOUSKI
Service de la bibliothèque

Avertissement

La diffusion de ce mémoire ou de cette thèse se fait dans le respect des droits de son auteur, qui a signé le formulaire *« Autorisation de reproduire et de diffuser un rapport, un mémoire ou une thèse »*. En signant ce formulaire, l'auteur concède à l'Université du Québec à Rimouski une licence non exclusive d'utilisation et de publication de la totalité ou d'une partie importante de son travail de recherche pour des fins pédagogiques et non commerciales. Plus précisément, l'auteur autorise l'Université du Québec à Rimouski à reproduire, diffuser, prêter, distribuer ou vendre des copies de son travail de recherche à des fins non commerciales sur quelque support que ce soit, y compris Internet. Cette licence et cette autorisation n'entraînent pas une renonciation de la part de l'auteur à ses droits moraux ni à ses droits de propriété intellectuelle. Sauf entente contraire, l'auteur conserve la liberté de diffuser et de commercialiser ou non ce travail dont il possède un exemplaire.

Se trouver au milieu des vagues a un côté onirique. Terreur et extase rôdent toutes deux ensemble, menaçant de submerger le rêveur.

Extrait de *Jours barbares*,

William Finnegan

REMERCIEMENTS

Je me rappelle l'époque, pas si lointaine, où ma compréhension de la dynamique des vagues s'apparentait davantage à l'émerveillement enfantin et pleinement suffisant de voir la surface de l'eau se rabattre sur elle-même avant de s'écraser contre la berge. C'était avant d'y jeter un oeil de plus près. De beaucoup plus près. Bien avant d'entrevoir cette complexité qui se cache derrière un phénomène pourtant si familier. C'était avant même d'envisager la présence de glace avec laquelle les vagues interagissent d'une manière tout aussi difficilement saisissable. Il m'aura fallu l'ensemble de ces dernières années pour comprendre que les vagues ne s'appréhendent qu'au prix d'efforts soutenus. Aujourd'hui, je constate n'avoir qu'effleuré un sujet d'étude aussi vaste que fascinant.

Ce travail n'aurait pu être accompli sans la participation de nombreuses personnes. Je tiens à remercier en premier lieu Cédric Chavanne et Dany Dumont pour la confiance accordée. À titre de superviseurs, ils m'ont offert une grande liberté dans la réflexion et la direction du travail accompli tout en me prodiguant une aide inestimable dans sa progression. J'ai beaucoup apprécié la constance et la créativité de l'un et l'autre qui se sont avérées être des forces fort complémentaires et précieuses. Ils ont su entretenir ma motivation tout au long de ces dernières années et m'alimenter d'idées nouvelles chaque fois que ma conviction vacillait. Un merci particulier également à James Caveen qui aura su non seulement décupler mes compétences informatiques, mais surtout contribuer à me forger une structure de travail consistante et efficace.

Je veux également remercier Andrea Scott qui m'a chaleureusement accueilli à l'Université de Waterloo afin de m'initier à la manipulation d'imagerie satellitaire. Ce fut en cette occasion que j'ai pu déterminer les premiers défis et enjeux reliés à la nature propre de mon projet de recherche. Ce fut également en cette occasion que purent être dégagées les premières données numériques orientant subséquemment l'ensemble de la recherche. Plus localement, je suis fort reconnaissant à Sylvain Joly, Simon Senneville et

Urs Neumeir d'avoir facilité l'accès à des jeux de données environnementaux et modèles numériques essentiels à la progression du travail.

De manière plus large, j'en profite pour saluer les membres du POLR qui forment un noyau de chercheurs dynamiques, passionnés et fort inspirants. Je tourne plus spécifiquement mes pensées vers mes collègues à la maîtrise, Jean-François Beaudoin, Karine Robert et Jean-Luc Shaw. Ce dernier fut également, à mon grand bonheur, mon voisin de bureau et une source d'inspiration constante en terme d'ingéniosité et de persistance.

Finalement, un dernier merci à Graig Sutherland et Daniel Bourgault qui ont accepté de lire et commenter ce mémoire.

RÉSUMÉ

Une nouvelle version de *Waves-in-Ice Model* (WIM) fut développée pour représenter un spectre de vague évoluant dans des conditions de fetch limité en présence de glace de mer distribuée le long d'un axe 1-D. Les termes source implémentés incluent le transfert d'énergie par le vent, la dissipation par déferlement, les échanges non linéaires vagues-vagues ainsi que l'atténuation par la glace. La forme du spectre est libre de contraintes ce qui permet son évolution en présence d'une couverture de glace partielle ou discontinue. Une calibration du modèle fut faite avec les données opérationnelles de WAVEWATCH III$^{\text{TM}}$, laquelle a nécessité de moduler les termes source par l'introduction de coefficients. Basées sur les images SAR de Sentinel-1 pour l'Estuaire du Saint-Laurent durant les périodes hivernales de 2016 à 2019, des distributions réalistes de glace furent établies correspondant à 3 cas spécifiques. Les vagues furent estimées au moyen des données de vent du Système Régional de Prévision Déterministe (SRPD). De ces données, des transects furent extraits et soumis au modèle. Les résultats obtenus furent comparés avec ceux d'AWAC mettant en évidence la nécessité de mobiliser davantage de données pour valider la méthode. La description et la validation du modèle sont présentées à l'intérieur du premier chapitre alors que l'intégration des données environnementales est détaillée dans le second.

Mots clés : vagues, glace, WIM, attenuation, spectre, Saint-Laurent, interaction non linéaire, SAR, fetch.

ABSTRACT

A new version of the 1-D Waves-in-Ice Model (WIM) has been developed to represent a wave spectrum evolving in fetch-limited waters with variable ice distributions. The source terms included in the model are energy gain from the wind, dissipation by white capping, nonlinear waves-waves interactions and ice attenuation. The shape of the spectrum is not constrained during growth which allows energy propagation in waters characterized by partial or discontinuous ice cover. Calibration was done with operational WAVEWATCH III^{TM} data which led to the inclusion of weight functions to modulate the source terms. The model was run for realistic cases. Based on Sentinel-1 SAR images for the St.Lawrence Estuary for the winter periods of 2016-2019, realistic ice distributions for 3 specific scenes have been investigated. Waves were estimated based on the wind field from the Canadian Regional Deterministic Prediction System (RDPS). Results were compared with observations showing large biases which provided avenues for further investigation. Description and validation of the model is presented in the first chapter while the second chapter integrates the environmental data.

Keywords : wave, ice, WIM, attenuation, spectrum, St. Lawrence Estuary, nonlinear interaction, SAR, fetch.

TABLE DES MATIÈRES

LISTE DES TABLEAUX

LISTE DES FIGURES

INTRODUCTION GÉNÉRALE

Contexte

La zone marginale de glace (MIZ) est la région confinée entre la banquise intérieure et les eaux libres. Significativement affectée par les vagues, elle se caractérise physiquement comme un agrégat de floes où se manifestent de nombreuses interactions entre l'océan, l'atmosphère et la glace. Ces interactions, bien que survenant à petite échelle, ont pourtant des impacts importants à large échelle (Williams et al., 2013a). En Arctique, par exemple, les vagues contribuent à la fracture de la glace et le développement de la MIZ qui, en retour, accélère la fonte estivale en raison de l'augmentation du périmètre total des glaces (Montiel et al., 2016).

De plus, les données récentes montrent un retrait généralisé de la couverture de glace en Arctique. L'étendue de la banquise tend à diminuer et la glace pluriannuelle se voit progressivement remplacée par de la glace de première année, plus mince (Stroeve et al., 2014). Cette tendance entraîne une augmentation de la proportion des eaux libres d'où en résulte la formation de vagues conséquemment plus importantes (Thomson and Rogers, 2014). Les études mettent également en lumière la plus grande variabilité de la couverture de glace sur une base annuelle (Holland and Stroeve, 2011) et l'accès aux zones de glace saisonnière (SIZ) est en augmentation en raison du réchauffement climatique (Stephenson et al., 2011). Or, la navigation et les activités économiques reliées au domaine maritime s'intensifient dans ces régions. Ce constat souligne la nécessité de modèles prévisionnels fiables. Toutefois, le rôle des vagues de gravité demeure difficile à comprendre, à quantifier, à modéliser et à implémenter dans les modèles actuels Williams et al. (2013a).

Une des raisons limitant la compréhension des interactions vagues-glace est la faible quantité de données disponnibles pour l'étude de ces interactions. De plus, une

majorité des mesures de vagues en présence de glace sont prises à des intervalles de plusieurs kilomètres voire plusieurs dizaines de kilomètres. Par exemple, les données de Meylan et al. (2014), tout comme celles de Doble et al. (2015), portant sur l'atténuation du spectre de vague en Antarctique, étaient espacées de quelques dizaines de kilomètres. Dans ce contexte, les mécanismes physiques intervenant à plus fine échelle ne peuvent être aisément caractérisés de manière quantitative. Représenter l'évolution du spectre de vague à une échelle de l'ordre de 10^2 m relève d'une première étape dans cette perspective. Pour ce faire, comprendre et représenter les manifestations physiques dominantes à la base de la modélisation est nécessaire.

De manière générale, la modélisation des vagues est un sujet d'étude qui a évolué considérablement au cours des dernières décennies. Sa représentation est généralement basée sur une équation d'action ou de transport d'énergie de la forme

$$\frac{DE}{Dt} = S_{\text{tot}} = (S_{\text{in}} + S_{\text{ds}}) + S_{\text{nl}} + S_{\text{ice}} + S_{\text{autres}} \tag{1}$$

où $E = E(x, y, f, \theta, t)$ est le spectre d'énergie des vagues, une fonction de la position (x, y), de la fréquence f et de la direction de propagation θ des vagues, et du temps t. La dérivée matérielle de E est égale à la somme S_{tot} de termes sources (Masson and Leblond, 1989), chacun exprimant le gain, la perte ou encore la redistribution d'énergie à l'intérieur du spectre associé à différents phénomènes physiques. Parmi les manifestations les plus courantes se retrouvent le transfert d'énergie par le vent S_{in} et la dissipation par déferlement S_{ds} qui sont généralement paramétrés ensemble, les interactions non linéaires entre les vagues S_{nl} ou encore l'atténuation par la glace S_{ice} lorsque celle-ci est présente. Davantage de phénomènes sont parfois représentés selon les contextes (regroupés ici sous S_{autres}), certains concernant directement les vagues (friction sur le fond, réfraction), d'autres concernant les interactions entre les vagues et la glace (collision entre les floes, fracture). Dans les sections suivantes sont rappelées les notions concernant les principaux termes sources qui seront décrits et utilisés dans

ce mémoire.

La génération des vagues par le vent

La représentation du transfert énergétique du vent sur les vagues S_{in} relève à la fois du défi théorique de représenter l'écoulement d'un fluide sur une surface variable dans le temps et l'espace, mais aussi celui de mesurer de manière directe l'impact du vent sur les vagues.

C'est Phillips (1957) et Miles (1957) qui formulèrent initialement l'idée d'un phénomène de résonance. En particulier, Miles présenta le premier mécanisme physiquement plausible décrivant une relation de résonance entre l'onde de pression atmosphérique et les vagues de surface. La représentation négligeait cependant les effets turbulents et des tentatives furent faites pour les intégrer. Plus récemment, les travaux de Snyder et al. (1981) et de Hasselmann and Bösenberg (1991) ont montré des transfers d'énergie d'ordre similaire avec la théorie de Miles, même si les taux prédits demeurent inférieurs aux mesures faites. De nombreuses déclinaisons du modèle de Miles (1957) sont encore utilisées de nos jours.

L'interaction entre les vagues

Le rôle des interactions non linéaires entre les vagues S_{nl4} fut, quant à lui, mis en évidence suite au *JOint North Sea WAve Project* (Hasselmann et al., 1973). C'est toutefois Hasselmann (1962), qui avait précédemment développé les prémisses de la représentation de l'interaction non linéaire entre les vagues, laquelle entraîne une redistribution de l'énergie à l'intérieur du spectre de vague en faisant intervenir des ensembles

de quatre composantes. L'intégrale de Boltzman (Hasselmann, 1962) est définie comme

$$S_{\mathrm{nl4}}(\vec{k_4}) = \iiiint T_1(\vec{k_1}, \vec{k_2}, \vec{k_1} + \vec{k_2} - \vec{k_4}) E(\vec{k_1}) E(\vec{k_2}) E(\vec{k_1} + \vec{k_2} - \vec{k_4}) d\vec{k}_1 d\vec{k}_2 \\ - E(\vec{k_4}) \iiiint T_2(\vec{k_1}, \vec{k_2}, \vec{k_4}) E(\vec{k_1}) E(\vec{k_2}) d\vec{k}_1 d\vec{k}_2 \quad (2)$$

où le nombre d'onde $\vec{k_4}$ est en interaction avec les autres composantes $\vec{k_1}, \vec{k_2}$ et $\vec{k_3} = \vec{k_1} + \vec{k_2} - \vec{k_4}$. Le choix des quadruplets impliqués repose sur les conditions de résonance (Eq. 3 et 4) exprimées en termes de nombres d'onde $\vec{k_i}$ et de fréquences f_i tel que

$$\vec{k_1} + \vec{k_2} = \vec{k_3} + \vec{k_4} \quad (3)$$

$$f_1 + f_2 = f_3 + f_4. \quad (4)$$

Les fonctions T_1 et T_2 sont des coefficients de transfert correspondant aux nombres d'onde impliqués. La balance entre les deux segments de l'équation 2 résulte en un gain ou une perte d'énergie pour la composante $\vec{k_4}$ évaluée, mais la somme des valeurs évaluées sur l'ensemble du domaine spectral est nulle puisque l'énergie n'est que redistribuée à l'intérieur du spectre. Conséquemment, l'évaluation de l'ensemble du terme source S_{nl4} est déterminé par l'évaluation de toutes les valeurs $S_{\mathrm{nl4}}(\vec{k_4})$ composant le spectre.

Tel qu'illustré à la figure 1, la forme du terme source S_{nl4} pour un spectre de vagues met en évidence le rôle des quadruplets dans la redistribution de l'énergie. L'énergie est transférée depuis les fréquences centrales vers les extrémités du spectre, entraînant la migration de la période modale vers les basses fréquences. Cette notion est fondamentale puisque l'ensemble des termes sources sont directement dépendants non seulement de la quantité d'énergie relative au spectre, mais plus spécifiquement de sa distribution.

La solution à l'intégrale de Boltzmann est toutefois fort exigeante en termes de temps de calcul, même avec la puissance des ordinateurs modernes. Elle n'est toujours

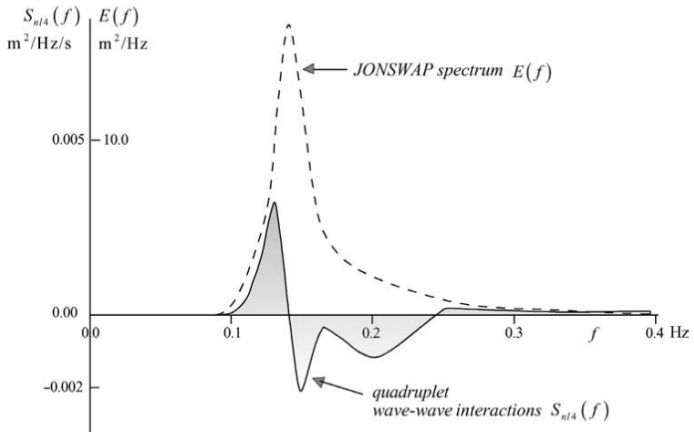

FIGURE 1: Terme source S_{nl4} pour les interactions non linéaires entre les vagues évalué d'après la méthode exacte de van Vledder (2006) pour des vagues de $Hs = 3.5$ m et $Tp = 7$ s. Figure de Holthuijsen (2007).

pas intégrée dans les modèles prévisonnels actuels et ce sont plutôt par des méthodes d'approximation que les interactions entre les vagues sont calculées. En particulier, Hasselmann et al. (1985) développèrent la *discrete interaction approximation* (DIA) pour évaluer les interactions non linéaires entre les vagues. L'intégration de la DIA dans les modèles de vagues entraîna le développement des modèles de troisième génération (3G) tels que WAM (The WAMDI group, 1988), SWAN (Booij et al., 1999) ou WAVEWATCH (Tolman, 1991), parmi les plus courants. Ces modèles considèrent un spectre de vagues bidimensionnel évoluant dans le temps et l'espace selon l'équation d'équilibre et sans contraintes sur la forme spectrale, mis à part certains limiteurs dans les hautes fréquences. Et, bien qu'inexacte, la DIA conserve certains éléments de la solution exacte. Elle permet notamment la migration de l'énergie vers les basses fréquences ainsi que la stabilisation du spectre pendant le développement des vagues.

Initialement développées pour les vagues en eaux profondes, des adaptations de la DIA furent ultérieurement proposées pour une utilisation en eaux peu-profondes. De plus, d'autres méthodes d'approximation furent progressivement avancées dans le but de toujours mieux représenter les échanges non linéaires. Diverses approches furent

envisagées telles que (1) la simplification de l'équation exacte, (2) l'amélioration de la DIA ou encore (3) le développement de nouvelles techniques. À ce jour, les méthodes dites exactes (WRT, GQM ou RIAM) font figure de références pour le développement de méthodes plus rapides (van Vledder, 2012). Toutefois des études comparatives sont toujours nécessaires pour tester les performances sur une base opérationnelle. La précision et l'applicabilité des méthodes sont encore ainsi soumises à la contrainte du coût de calcul. Il n'en reste pas moins que chacune de ces approches développées pour estimer les interactions non linéaires entre les vagues ont en commun d'impliquer une connaissance bidimensionelle du spectre d'énergie.

La dissipation énergétique

La dissipation énergétique S_{ds}, quant à elle, représente la manifestation physique la moins bien comprise dans la modélisation du spectre de vague. Un consensus général attribue cependant au déferlement un rôle prépondérant à cette fin en présence de vents forts à modérés. Il est d'ailleurs généralement accepté que S_{ds} est fonction du spectre de vague E tel que

$$S_{\mathrm{ds}} \sim E^n \tag{5}$$

mais il n'est pas acquis que la relation est linéaire ($n = 1$), certains modèles considérant des valeurs où $n = 2, 3$ ou même 5.

De nombreuses études présentent différentes approches analytiques. Aucune d'elles cependant ne traite directement de la physique du déferlement responsable de la dissipation (Cavaleri et al., 2007). Elles suggèrent plutôt des hypothèses pour interpréter le comportement instable précédent le déferlement ou encore le spectre résultant du déferlement. De plus, toutes les hypothèses sur lesquelles reposent les différents modèles manquent de données expérimentales à des fins de validations.

Toutefois, la représentation mathématique la mieux développée, et encore fréquemment utilisée dans les modèles de dissipation, est due à Hasselmann (1974) et considère une représentation linéaire. De plus, Komen et al. (1984) démontrèrent la possibilité de calibrer une forme spectrale pour la dissipation en considérant la balance de tous les termes sources. Plus récemment, Young and Babanin (2006) ont mis en lumière que les composantes obliques sont supérieures à celles associées à la direction principale des vagues et, par conséquent, le déferlement contraint le spectre directionnel à une bande spectrale étroite.

L'atténuation par la glace

L'intégration de la glace dans les modèles fut faite pour la première fois par Masson and Leblond (1989) qui inclurent les effets de la glace à l'intérieur de la fonction de transport de l'énergie qui n'était utilisée jusqu'alors qu'en situations d'eau libre de glace.

Les modèles actuellement utilisés pour représenter l'atténuation des vagues par la glace S_{ice} se divisent en deux catégories. Dans le premier cas de figure, les modèles de dispersion considèrent une succession de réflexions à la base de la dispersion énergétique. Ces réflexions sont la conséquence des rencontres entre les vagues et les fronts de glace. Cette représentation est, par conséquent, fortement reliée à la distribution de taille des floes (FSD). Dans le deuxième cas, les modèles visqueux considèrent les zones de glace comme une ou plusieurs couches où l'énergie des vagues est atténuée sous la forme d'une dissipation visqueuse. Les modèles visqueux sont donc indifférents de la FSD.

De nombreuses études ont montré que l'énergie des vagues décroît de manière exponentielle proportionnellement à la distance x parcourue sous le couvert de glace

(Wadhams, 1978). L'énergie d'un spectre de vague E_0 diminue tel que

$$E(x) = E_0 e^{-\alpha x} \tag{6}$$

où $\alpha(f, A, h)$ est le terme d'atténuation, lequel dépend à la fois de la fréquence des vagues (les courtes vagues sont atténuées rapidement alors que les vagues longues voyagent beaucoup plus profondément sous la couverture de glace), de la concentration A de la glace, et de l'épaisseur de glace h (Li et al., 2017; Sutherland et al., 2019).

Enjeux

De nombreuses études se sont penchées sur l'atténuation des vagues par la glace par le passé (Wadhams, 1978; Squire and Moore, 1980; Wadhams et al., 1988; Liu et al., 1991). Toutefois, la distance séparant les données prélevées se situent dans un ordre de grandeur de quelques dizaines de kilomètres voire davantage. Même les études récentes (Meylan et al., 2014; Doble et al., 2015) portent un regard sur l'atténuation des vagues par la glace pour des zones de plus de 100 km avec un nombre réduit de mesures. Ce faisant, les mécanismes physiques intervenants entre deux points de mesure sont difficilement quantifiables et l'hypothèse de stationarité probablement enfreinte .

Les premiers modèles prévisionnels incluant de la glace de mer étaient fort simplistes alors que la MIZ était traitée soit comme de l'eau libre sinon comme une zone imperméable (Tuomi et al., 2011). De nombreux efforts ont depuis été déployés afin d'intégrer les effets des vagues dans la physique des modèles (Collins et al., 2015). Les processus physiques contribuant à l'atténuation sont nombreux. Les seuls processus dissipatifs incluent, par exemple, la déformation inélastique de la glace, la fracture des floes, les collisions, le franchissement ou la turbulence (Montiel et al., 2016). La contribution relative de ces mécanismes est généralement inconnue et l'estimation de l'effet de ces processus sur l'énergie des vagues est un enjeux actuel. Même si de nombreuses

paramétrizations empiriques linéaires furent développées pour représenter la MIZ, leur validité n'est pas établie et la calibration représente un défi de taille limité notamment par la disponibilité des données (Mosig et al., 2015).

Encore aujourd'hui, la collecte de données in situ pour permettre l'étude des interactions entre les vagues et la glace demeure un défi. En effet, que ce soit pour la glace ou pour les vagues, les données doivent être représentées soit à l'intérieur d'un champ spatial sinon le long d'un transect orienté (ou projeté) dans la direction principale des vagues afin de pouvoir en suivre l'évolution. Cependant, avec la puissance croissante des ordinateurs, et considérant la résolution toujours plus fine des modèles, la nécéssité de mieux représenter la physique à l'intérieur de la MIZ demeure un enjeu actuel. Le besoin de générer de nouveaux jeux de donnée afin d'étudier ces interactions relève donc une nécessité actuelle. Dans cette optique, la disponibilité grandissante d'imagerie satellitaire, en particulier celle des images à synthèse d'ouverture (SAR), offre de plus en plus d'opportunités de représenter et caractériser la distribution de glace de mer et, conséquemment, d'en étudier les interactions avec les vagues.

L'estuaire maritime du Saint-Laurent

La zone ciblée pour mener notre étude et mieux documenter les interactions vagues-glace est la région subarctique de l'estuaire maritime du Saint-Laurent (LSLE), Canada. La région est caractérisée par la présence de glace saisonnière entre les mois de décembre et avril. La portion occidentale de l'estuaire maritime est le théâtre d'une polynie dite de chaleur sensible induite par la résurgence des eaux chaudes de l'Atlantique remontant le chenal Laurentien jusqu'à sa tête, près de l'embouchure du fjord du Saguenay et de la ville de Tadoussac (J Saucier et al., 2003). Ces particularités physiques et environnementales font de l'estuaire maritime du Saint-Laurent une zone favorable à la génération de vagues en hiver, et la propagation de celles-ci à travers des conditions de glace variées.

Objectifs

Les objectifs guidant la rédaction de ce mémoire diffèrent largement des objectifs initialement fixés. L'orientation originelle du projet visait à utiliser un jeu de données issu de radars hautes-fréquences de type WERA pour la mesure des vagues. Ce faisant, la représentation spatiale, étendue sur une zone de quelques dizaines de kilomètres au large de l'estuaire du Saint-Laurent, offrait l'avantage d'exposer continûment, dans l'espace et dans le temps, l'état des vagues dans la zone. La comparaison avec l'imagerie satellitaire pour établir la distribution de glace aurait permis la superposition de ces jeux de données présentés sous forme de champ, et aurait permis de déterminer la validité d'une telle approche novatrice dans l'étude des interactions vagues-glace. Cependant, la difficulté à obtenir des données de vagues en présence de glace pour les hivers 2015 à 2019, et plus particulièrement pour les périodes spécifiques pour lesquelles des images de glace étaient disponibles a forcé des ajustements dans les objectifs ainsi que dans la méthodologie du projet en lui-même. En effet, la portée des radars est très limitée en présence de glace et la mesure des vagues requiert un certain niveau d'énergie des vagues (Wyatt et al., 2011). L'analyse préliminaire des données disponibles a mis en évidence la difficulté à valider ces données et à les intégrer dans le contexte de l'étude envisagée. Une réorientation des objectifs fut entreprise.

L'actualisation des objectifs fut faite de manière à recentrer le projet autour de la modélisation et plus particulièrement vers la capacité à reproduire l'évolution d'un spectre de vague en présence d'une couverture partielle de glace. Les objectifs actualisés sont donc :

1. le développement et la calibration d'un modèle de vague 1D en eaux profondes, lequel permet à un spectre de vague d'évoluer librement sous l'effet combiné des termes source découlant du forçage par le vent, des interactions vagues-vagues et de la dissipation par déferlement, mais aussi de la dissipation par la glace. La motivation

du choix d'un modèle 1D repose sur la simplicité et la flexibilité d'un tel caneva pour l'étude de phénomènes spécifiques comme Dumont et al. (2011) pour la fracture de la glace ou encore Bismuth (2014) pour la sensibilité à la distribution du volume de glace ;

2. l'intégration des images radar de glace avec les données environnementales pour caractériser quantitativement la distribution spécifique de glace dans le but d'étudier les interactions vagues-glace en présence d'une couverture de glace variable en épaisseur et concentration.

La motivation à la base de ce travail repose à la fois sur le besoin de mieux comprendre la nature complexe des interactions entre les vagues et la glace de mer, mais aussi sur la composante méthodologique du projet. Ce dernier élément s'inscrivant dans le contexte du défi collectif d'élargir l'éventail des sources de données utiles pour ce faire.

Le présent mémoire est divisé sous la forme de deux articles scientifiques. Le premier article, *A one-dimentional spectral wave model for studying wave-ice interactions in fetch-limited environments*, porte sur la description et la calibration du modèle développé pour étudier l'évolution du spectre de vague sous la contrainte du vent. Le second article, *Study of wave-wave interactions in the St.Lawrence estuary using SAR imagery and wave modeling*, porte sur l'intégration des données environnementales pour forcer le modèle dans des configurations 1D.

CHAPITRE I

A ONE-DIMENSIONAL SPECTRAL WAVE MODEL FOR STUDYING WAVE-WAVE NONLINEAR INTERACTIONS IN FETCH-LIMITED ENVIRONMENTS

Abstract

Studying coupled wave-ice interactions is sometimes best achieved with simple, light-weight models that incorporate the relevant physics in idealized to more realistic configurations. From a previous Waves-in-Ice Model (WIM) version, new parametrizations focusing on wave generation have been implemented. The proposed new version allows the wave spectrum to grow and evolve under wind stress and the wave energy to be transferred through nonlinear wave-wave interactions. Validation with operational WAVEWATCH III^{TM} (WW3) in open water permitted to set parameters for the Lower St. Lawrence Estuary fetch-limited waters. To succeed reproducing WW3 results, a set of weights has been added to modulate the source terms. Thus, the resulting version allows energy to be transferred from the atmosphere to the ocean along a one dimensional spatial grid. Such addition may be essential to study waves-ice interaction in regions where ice cover is mostly partial and variable in the St.Lawrence Estuary. Model parameterizations and settings are described in the present paper.

1.1 Introduction

The first order effect of ice on waves is attenuation. It has been shown by observations (Wadhams et al., 1988; Doble et al., 2015; Meylan et al., 2014) that waves attenuate at a frequency-dependent rate, with short waves attenuated more rapidly

than longer waves. Dumont et al. (2011) implemented a 1-D attenuation model together with an ice break-up parameterization. The choice of a 1-D model rather than a 2-D model was motivated by the simplicity of it to isolate and study specific features. This model was further improved by Williams et al. (2013a,b). These models were meant to evaluate the extent and floe size distribution of the marginal ice zone. They did not include wind generation. Bismuth (2014) included wind generation and dissipation through white capping and studied how the spatial distribution of ice affected the wave spectrum in a given overall ice concentration and with a given wind stress. His model however was not compared with observations and did not include wave-wave interactions that are key to provide the right spectral shape. In this paper, we further develop the one-dimensional model of Bismuth, which is largely based on Williams et al. (2013a), to account for quadruplet interactions in the perspective to study how the wave spectrum evolves along transects in which sea ice is distributed according to observations.

This paper aims to present a one-dimensional wave model integrating wave-wave nonlinear interactions. Development of the model is based on a directional energy spectrum being advected along a one-dimensional spatial grid. Physical processes taken into consideration include energy input by the wind, nonlinear wave-wave interactions and energy dissipation associated to white capping. While all source terms implied are focusing on open water processes at this stage, the advection scheme is largely based on Williams et al. (2013a) opening the perspective of including more source terms, thus studying deep water wave propagation under variable ice cover. The energy sources or sinks related to those processes are functions of the 2-D energy spectrum. From WW3 output dataset ran for the lower St. Lawrence estuary (LSLE) were depth is generally over 100 meters (Ruest et al., 2016), a calibration of the model has been applied where focus has been put on significant wave height H_s and peak period T_p. This led to include weight factors on every source terms in order to obtain comparable H_s and T_p values between WW3 and the 1-D model predictions.

The first section describes the 1-D model, addressing related theoretical notions. The second section displays the specific configuration settings of the model including the initialization. Results are presented in section three highlighting the implications of the nonlinear wave-wave interaction. Applications, limitations and perspective of the model are discussed in section five.

1.1.1 Energy balance equation

Based on Williams et al. (2013a), the energy balance equation in WIM in the absence of background currents is given by

$$\frac{1}{c_g} D_t E = (1 - A)(S_{\text{in}} + S_{\text{ds}}) + A S_{\text{ice}} + S_{\text{nl}} \tag{1.1}$$

where c_g is the group speed and $D_t E$ the material derivative of the energy spectrum $E = E(f, \theta)$. The source terms S_{in}, S_{ds} and S_{nl} denote respectively the atmospheric input of energy by the wind, the energy loss due to dissipative processes and the nonlinear energy transfers from the wave-wave conservative interactions. The nonlinear Benjamin-Feir instability (Collins et al., 2015) which transfer may occur in 1-D waves based on wave steepness and spectral bandwidth is also ignored. Here, the S_{ds} source term is restricted to white capping and S_{ice} refers to ice processes. In presence of ice, S_{in}, S_{ds} and S_{ice} are weighted according to the ice concentration $A \in [0, 1]$ while dispersion relation is assumed to not change and thus S_{nl} applies in both open water and under ice cover. Considering that WIM aims to evaluate wave propagation in deep water ($kH \gg 1$) and calibrated for the fetch-limited LSLE where depth is generally over 100 m(Ruest et al., 2016), bottom friction and nonlinear three-wave interactions (triads) are ignored.

While WIM has been developped to study wave-ice interactions, the focus of this paper is on open water waves only, thus the ice concentration $A = 0$ and Equation 1.1

becomes

$$\frac{1}{c_g} D_t E = S_{\text{in}} + S_{\text{ds}} + S_{\text{nl}}. \tag{1.2}$$

The different source terms are described separately below.

1.1.2 Wind input and dissipation source term

The representation of the input and dissipation source term is based on separate processes but are generally interrelated and balanced. More specifically, those defined in WIM are the ones evaluated in SWAN (Booij et al., 2006) or associated to ST1 flag in WAVEWATCH III (Tolman, 2009).

1.1.2.1 Wind input source term

The wind input source term S_{in} is assumed here to be a mechanism where waves are generated by resonance between air pressure fluctuations propagating at the water surface. This is based on Miles (1957) expression with a term α added to initialize wave growth such that

$$S_{\text{in}} = \alpha + \beta E \tag{1.3}$$

leading to a source term expressed as a linear function of E. The coefficient β is the positive feedback that allows the wave spectrum to exponentially grow in time. The chosen representation relies on the theory presented by Snyder et al. (1981) where

$$\beta = 0.25 \frac{\rho_a}{\rho_w} \Big[28 \frac{u_*}{c_p} \cos(\theta - \theta_0) - 1 \Big] \omega \tag{1.4}$$

for ρ_a=1 and ρ_w=1025 being the air and water densities (kg/m^3), c_p the phase velocity, u_* the wind friction and $\omega = 2\pi f$, the orbital frequency. When waves are growing, the airflow is thus affected and the wind-induced pressure wave is then modified so the resonance is enhanced. Here

$$u_*^2 = C_D U_{10}^2 \tag{1.5}$$

for a wind velocity U_{10} at 10 m elevation blowing in the θ_0 direction and the drag coefficient C_D is given by the expression from Wu (1982) as

$$C_D = \begin{cases} 1.2875 \times 10^{-3} & \text{for } U_{10} < 7.5 \text{ m/s} \\ (0.8 + 0.065 U_{10}) \times 10^{-3} & \text{for } U_{10} \geq 7.5 \text{ m/s}. \end{cases}$$

When the ocean is calm and $E \approx 0$, the constant wind-wave growth term α from Cavaleri and Rizzoli (1981) is applied as

$$\alpha = \frac{1.5 \times 10^{-3}}{2\pi g^2} u_*^4 G \tag{1.6}$$

with $g = 9.81$ m/s^2 being the gravitational acceleration and G a cut-off function used to avoid growth in the low frequencies (Tolman, 1992). This modulating function is given by

$$G = e^{-(\frac{\omega}{\omega_{PM}})^{-4}} \tag{1.7}$$

related to the Pierson–Moskowitz frequency

$$\omega_{PM} = 2\pi \frac{0.13g}{28 u_*}. \tag{1.8}$$

In oceanic models, α is often ignored because wave energy is always present at low frequency and the resulting α term which plays a trigger role becomes negligible.

However, in a fetch-limited context whereas ice cover is present and attenuates energy, this part is requisite in the representation of wave growth.

1.1.2.2 The dissipation source term

While dissipation may be caused by many processes, the only source taken into consideration in WIM is the white-capping being the main mechanism attributed for dissipation in deep water. The S_{ds} representation used is the one presented by The WAMDI group (1988) based on the shape of the spectrum as

$$S_{\text{ds}} = -\mu k E \tag{1.9}$$

where

$$\mu = C_{wc}(\frac{\bar{s}}{\bar{s}_{PM}})^{p}\frac{\bar{\omega}}{\bar{k}} \tag{1.10}$$

with coefficients $p = 4$ and $C_{wc} = 2.36 \times 10^{-5}$ being tuneable parameters set according to Komen et al. (1984) while $\bar{s}$ is the mean steepness defined as $\bar{k}\sqrt{m_0}$ where m_0 is the zeroth moment of the spectrum. Specific value for Pierson–Moskowitz spectrum is 0.055 . Mean values $\bar{\omega}$ and $\bar{k}$ are for frequency and wave number.

1.1.3 Wave-wave interactions source term

Nonlinear wave-wave interactions play a significant role in the evolution of the energy spectrum in deep water (Tolman and Krasnopolsky, 2004; Young ; and van Vledder, 1993; Resio and Perrie, 2008; Hasselmann et al., 1985; Komen et al., 1984) and the importance of the mechanism is especially relevant when waves are developing under wind stress. Those interactions are known to be the lowest order mechanism to shift energy through frequencies and are mainly responsible for the migration of the

energy peak toward the lower frequencies. Nonlinear wave-wave interactions are also responsible for shape stabilization (van Vledder, 2012).

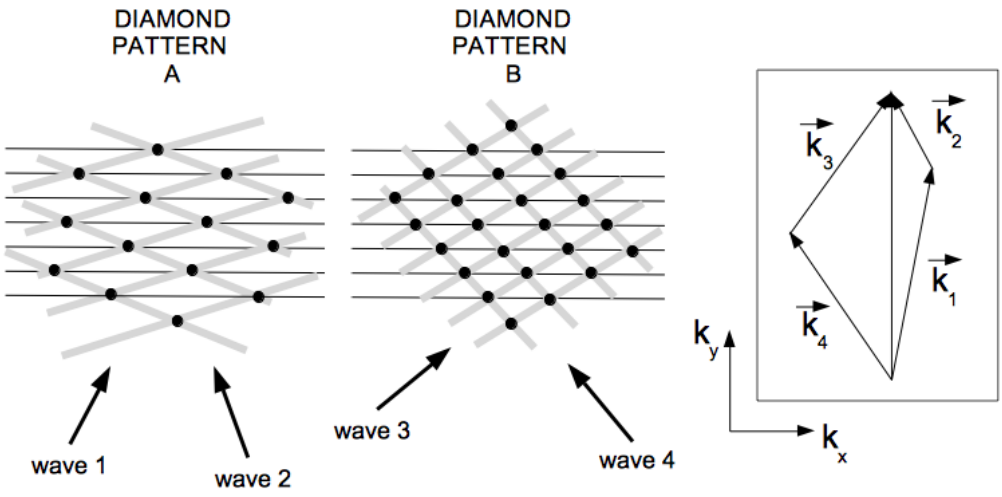

FIGURE 2: Diamond patterns resulting of two pair of waves. Black lines represent wave crests/troughs and black circles pattern crests/troughs. Box shows the four wave component in the k-space representation (with resonance condition 1.11 satisfied here). Image modified from Holthuijsen (2007).

As shown in Figure 2, in presence of two wave components with different lengths and directions, the interaction between those two component drives the creation of a diamond pattern characterized by his own crests and troughs and thus length, speed and direction. Such patterns would resonate with other pairs of wave components if the diamond patterns result with the same wave numbers $\vec{k}$ and frequency f. That can be summarized according to the two following resonance conditions :

$$\vec{k_1} + \vec{k_2} = \vec{k_3} + \vec{k_4} \tag{1.11}$$

$$f_1 + f_2 = f_3 + f_4 \tag{1.12}$$

where k_i and f_i are the wave number and frequency of each wave component. The four wave number vectors are also known as quadruplets. The exact formulation of those

interactions is obtained by the following Boltzmann integral (Hasselmann, 1962)

$$S_{\mathrm{nl4}}(\vec{k_4}) = \iiiint T_1(\vec{k_1},\vec{k_2},\vec{k_1}+\vec{k_2}-\vec{k_4})E(\vec{k_1})E(\vec{k_2})E(\vec{k_1}+\vec{k_2}-\vec{k_4})d\vec{k}_1 d\vec{k}_2 \\ - E(\vec{k_4}) \iiiint T_2(\vec{k_1},\vec{k_2},\vec{k_4})E(\vec{k_1})E(\vec{k_2})d\vec{k}_1 d\vec{k}_2 \quad (1.13)$$

with $\vec{k_4}$ as the vector wave number source term component interacting with the other wave components $\vec{k_1}, \vec{k_2}$ and $\vec{k_3} = \vec{k_1} + \vec{k_2} - \vec{k_4}$ according to the resonance conditions (Eq. 1.11 and 1.12). Functions T_1 and T_2 are transfer coefficients of the wave numbers implied. The balance between the two parts of the equation results either in a energy gain or loss.

Calculating all resonance pairs is very expensive even with present day computer technologies. Consequently, approximations have to be done operationally to evaluate nonlinear energy exchange between waves.

1.1.3.1 Discrete interaction approximation (DIA)

The S_{nl} source term used in WIM relies on the discrete interaction approximation (DIA) where only one set of all possible resonant configurations is required to evaluate energy density exchange between the four wave number vectors implied in the Boltzmann integral. Developed and described by Hasselmann and Hasselmann (1985), the essential feature of the DIA is that $k_1 = k_2 = k$ while k_3 and k_4 are related by an empirical shape parameter λ such that Eqs 1.11 and 1.12, expressed in terms of frequencies, become

$$f^+ = f_3 = (1+\lambda)f \quad (1.14)$$

$$f^- = f_4 = (1-\lambda)f \quad (1.15)$$

and exchanges are quantified according to the equation

$$\begin{pmatrix} \delta S_{\mathrm{nl}} \\ \delta S_{\mathrm{nl}}^{+} \\ \delta S_{\mathrm{nl}}^{-} \end{pmatrix} = \begin{pmatrix} -2 \\ 1 \\ 1 \end{pmatrix} C g^{-4} f^{11} \left[E^2 \left(\frac{E^+}{(1+\lambda)^4} + \frac{E^-}{(1-\lambda)^4} \right) - \frac{2EE^+E^-}{(1-\lambda^2)^4} \right] \tag{1.16}$$

where $E = E(f, \theta)$ is the total energy density of the spectrum attributed to each set of components and $\delta S_{\mathrm{nl}} = \delta S_{\mathrm{nl}}(f, \theta)$ is the energy exchanged. Values E^+ and E^- are referring to $E(f^+, \theta^+)$ and $E(f^-, \theta^-)$. The constant g is the gravitational acceleration while $C = 3 \times 10^{-7}$ and $\lambda = 0.25$ are parameters set empirically. Figure 3 shows the distribution of the wave numbers fitting the resonance conditions in the k-space. In a geometric perspective, the possible sets of wave numbers fitting the resonance conditions and shape parameter are $\theta^+ = 11.4°$ and $\theta^- = -33.6°$ relatively to $\vec{k}$.

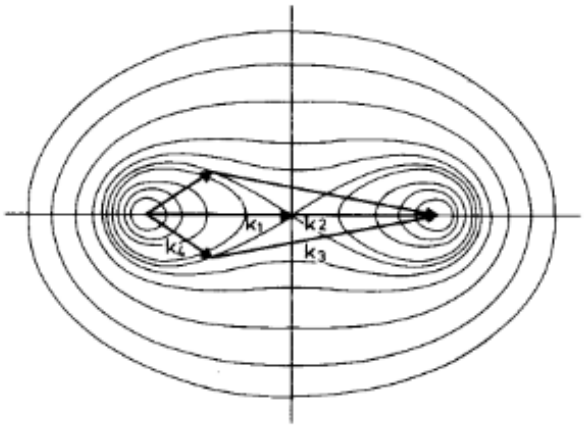

FIGURE 3: Interaction space diagram for DIA. Contour lines represent the possible end points of $\vec{k_1}$ and $\vec{k_4}$. Orientation relative to $\vec{k}$ between wave numbers for $\lambda = 0.25$ is $\theta_3(\theta^+) = 11.5°$ and $\theta_4(\theta^-) = -33.6°$. Image from Hasselmann et al. (1985).

A fundamental aspect of wave-wave interactions is that it involves waves travelling in different directions. That must be somewhat described. This was not the case in the one-dimensional wave propagation model used to study wave-ice interactions. This will

be discussed in the next section.

1.1.4 Model initialization

In WIM, a directional energy spectrum is developing along a one-dimensional grid starting from an initial wave spectrum E_0 which can be set according to significant wave height H_s and peak period T_p given as inputs (when no data are provided, E_0 is set to 0). According to those values, the creation of the 1-D JONSWAP spectrum $E(f)$ from Hasselmann et al. (1973) but reformulated by Goda (1988) based on a statistical analysis as

$$E(f) = \alpha H_s^2 \frac{f_p^4}{f^5} exp\Big[\frac{-5}{4}\Big(\frac{f_p}{f}\Big)^4\Big]\gamma^{exp\Big[\frac{-(f-f_p)^2}{2\sigma^2 f_p^2}\Big]} \tag{1.17}$$

where γ is a peak enhancement factor (set here to 3.3), $\alpha = 0.2044$ is a constant based on parameter γ and f_p the peak period. The 2-D directional spectrum is obtained as

$$E_0(f,\theta) = E(f)D(f,\theta) \tag{1.18}$$

where $D(f,\theta)$ is a spreading function that redistributes spatially the energy according to the wave frequency. Here, a Mistuyasu-type spreading function (Mitsuyasu et al., 1975) has been preferred amongst many because it provides the flexibility to be calibrated according to the nature of the waves and it is widely used in various wave engineering problems (Goda, 1999). It is defined as

$$D(f,\theta) = \frac{2^{2s-1}}{\pi}\frac{\Gamma(s+1)^2}{\Gamma(2s+1)}\cos\left(\frac{\theta-\theta_0}{2}\right)^{2s} \tag{1.19}$$

where Γ is the gamma function and

$$s(f) = \begin{cases} s_{\max}\left(\frac{f}{f_p}\right)^5 & \text{if } f \leq f_p, \\ s_{\max}\left(\frac{f}{f_p}\right)^{2.5} & \text{if } f > f_p \end{cases} \tag{1.20}$$

and the spreading parameter $s_{\max}$ is set to 10 as proposed by Goda and Suzuki (1975) for wind waves while f_p is the peak frequency. The adimensional shape of the directional spectrum resulting is shown in Figure 4. Specific Hs and Tp values used for initialization

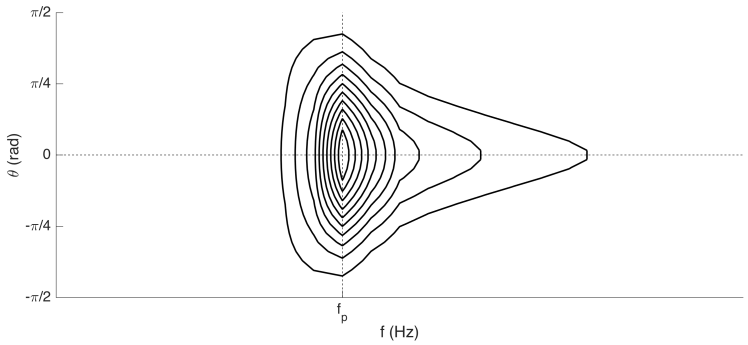

FIGURE 4: Initial two dimensional E_0 JONSWAP spectrum shape. The spectrum is defined from (-π,π) but, consequently to the spreading function shape, resulting energy is decreasing significantly with θ increasing and is almost null for $|\theta| > \pi/2$.

in the present paper are described in section 1.2.3.

1.2 Datasets and methodology

Validation of this WIM new version in open water has been done with WAVEWATCH III^{TM} (WW3). WW3 is a WAM-type third generation wave model widely used to study and predict waves in oceanic models. The model has been developed by the NOAA/NCEP and has been widely and successfully applied in global and regional scale studies (Tolman et al., 2013; Tang et al., 2008), for example, as in the real-time short-term BIO forecasting system for the eastern Canadian waters (Tang et al., 2008).

1.2.1 WW3 dataset extraction

Simulations over the LSLE for the period of 2012-2015 were done with a 5km resolution configuration of the WW3 operational wave model (version 5.03) applied to the EGSL domain. Wave entering the domain (Cabot and Belle-Isle Straits) were generated by a WW3 North-Atlantic configuration with a resolution of 38 km for water level and currents and forced by the Climate Forecast System Reanalysis (CFSR). Wind forcing is from Regional Deterministic Prediction System (RDPS) atmospheric model which is implemented operationally at the Canadian Meteorological Center (Smith et al., 2013). Currents were from the 5km resolution regional coupled ice-ocean circulation model for the Gulf of St. Lawrence developed and validated by J Saucier et al. (2003). In those simulations, water was free of ice and hourly wave and wind data output from 5×5 km grid were used to reconstruct transects.

Time periods were identified where the wind velocity was steady and offshore. Waves during these periods were also visualized to ensure significant waves height was monotonically increasing and the corresponding gradient oriented in the same direction as the wind. Wind and wave data 9 hours prior to the selected transects were also analyzed to ensure uniformity of the wave and wind fields in time. An example (Figure 5) used to validate transect quality is presented to show the wind and wave values along one of those transects.

In total, 49 transects fulfilling these criteria were obtained. Significant wave height (H_s), peak period (T_p) and wind velocity (U_{10}) were linearly interpolated on a one-dimensional grid along the transects with a spatial resolution of 500 m. to further compare waves growth in a higher resolution. The choice of the resolution was set based on Bismuth (2014) previous WIM version (even if later development in this actual WIM version led to increase the resolution to 100 m.). Distance from the shore has been evaluated according to the 2011 Canadian coastline from Statistics Canada.

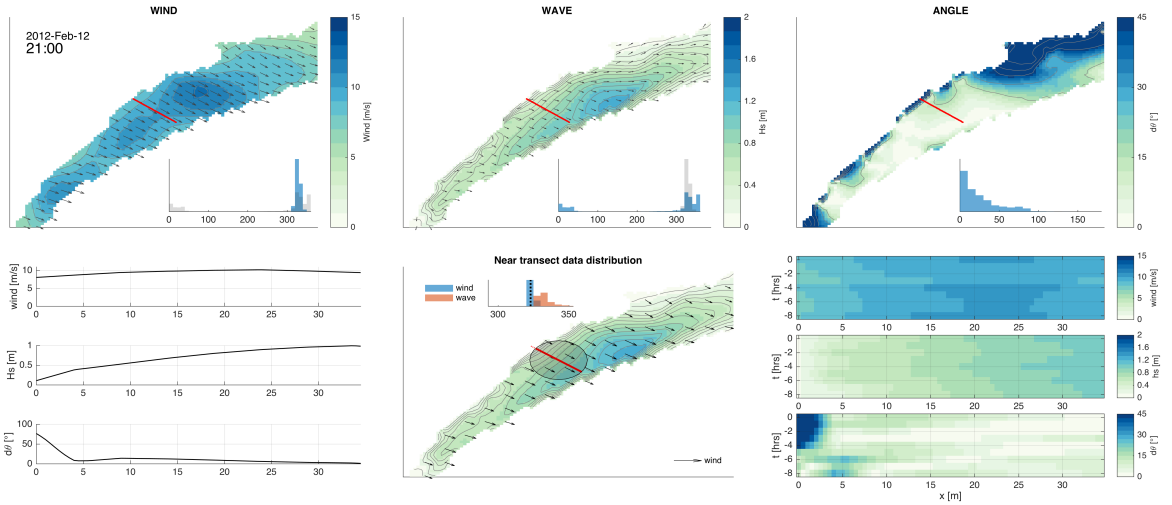

FIGURE 5: Example of the WW3 control panels used in the extraction of the transects. The upper row shows the wind field (left), wave field (center) and angular difference between both (right). The lower row shows data along the transect (left), distributions of wind and wave angles in the transect neighbourhood (center) and the evolution in time of the data (right).

No extrapolation was done near coastal boundaries, so most values in the very first kilometres are ignored.

1.2.2 Setting domain boundaries with GENER

To ensure that wave growth was mainly driven by sea wind, significant wave heights from WW3 were compared to the fetch model GENER (Neumeier et al., 2013) forced by a constant and unidirectional wind field. The model is a parametric wave model developed in the early 1980's and used to study wave climate over the St. Lawrence estuary. It predicts waves (H_s, T_p and direction) according to the time evolution of the wind over the region.

The wind velocity was set according to the WW3 mean velocity along every transect while the direction was assumed to be in the same orientation of the transect. This

assumption is realistic based on the criteria used to previously select transects. The parameterization for fetch-limited wind generation used in GENER was the Coastal Engineering Manual (CEM-03), as suggested by Neumeier et al. (2013) who optimized the model for the St. Lawrence Estuary.

Only transects at least 40 km long and with a relative root-mean-square error (rRMSE) less than 15 % for H_s between WW3 and GENER were kept and further referenced as transects of interest (TOI). In total, 25 TOI were selected. While every TOI ranges from $x = 1$ to $x = 54$ km from the coast, values between 10.5 and 40.5 km were represented by all TOI. As shown in figure 6, mean wind values for TOI dataset goes from 7.8 to 13.7 m s^{-1} but weigh more towards the lower values, especially around 11.5 m s^{-1}. Standard deviation ranges from 0.2 to 1.6 meters. The whole transect dataset is presented in figure 7.

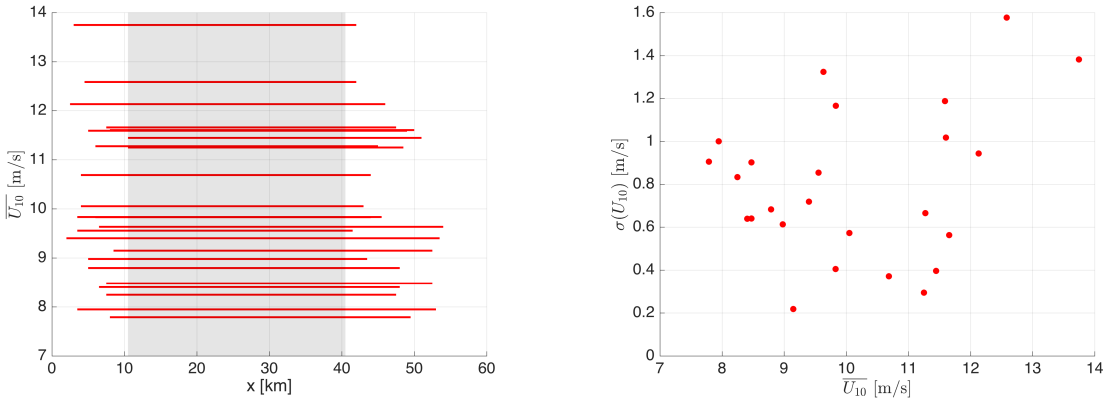

(a) Mean wind values for each transect

(b) Standard deviation

FIGURE 6: Transects of interest (TOI) distribution according to (left) the distance from the coast and wind speed for the 2012-2015 period and (right) wind standard deviation for each transect. Red lines and markers represent the transects and the grey shade limits the area where all transects data were available.

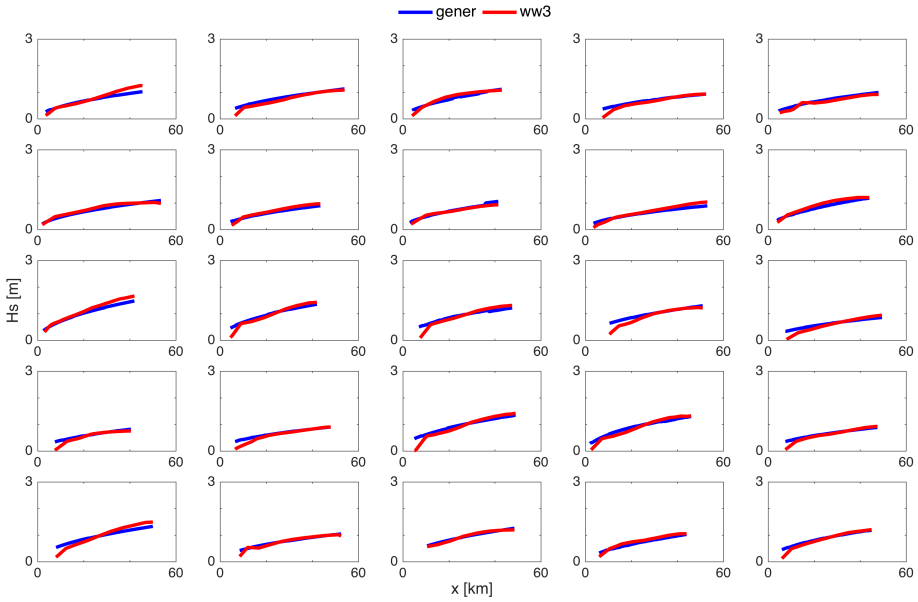

(a) Hs (m)

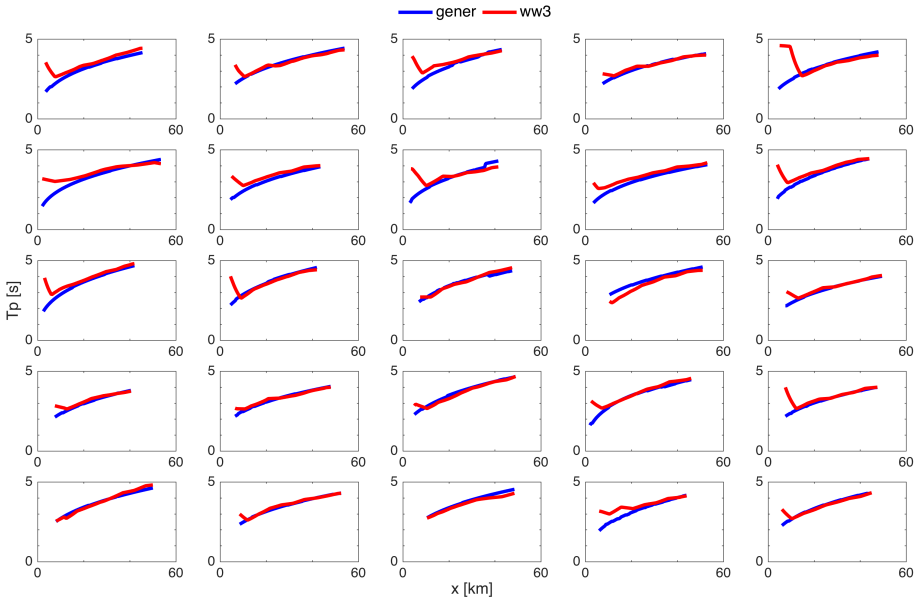

(b) Tp (s)

FIGURE 7: The WW3 transects with rRMSE with GENER lower than 15%, providing the database for later validation with WIM. Blue lines are for GENER and red lines are for WW3.

1.2.3 WIM settings and configuration

Based on data from WW3 at the beginning of every TOI, a 2-D directional spectrum was generated and used in WIM as initial spectrum $E_0 = E(x = 0)$. Since the exact form of the WW3 energy spectrum was not known, a specific spectrum shape had to be defined. Based on WMO (1998), a peak period T_p^* was evaluated from the initial H_s. The two parameters are related considering the mean steepness of a fully-developed wave spectrum by the relation

$$T_p^* = \sqrt{\frac{H_s}{a}}. \tag{1.21}$$

with $a = 0.04$ m/s^2.

The initial wave spectrum acts like a trigger to allow energy exchanges and spectrum to grow. While it is likely that the WIM and WW3 initial spectra do not present the same shapes, the choice of generating such spectra is mostly operational but supported by the role of the nonlinear wave-wave interactions that stabilize the shape of the spectrum and thus redistribute the energy accordingly among the spectrum.

1.2.4 Source terms weighting and model configuration

To obtain comparable results between WIM and WW3, it was necessary to add weights to S_{in}, S_{nl} and S_{ds}. From equation 1.2, this led to represent the energy balance equation without ice ($A = 0$) such as

$$\frac{1}{c_g} D_t E = W_{\mathrm{in}} S_{\mathrm{in}} + W_{\mathrm{ds}} S_{\mathrm{ds}} + W_{\mathrm{nl}} S_{\mathrm{nl}}. \tag{1.22}$$

with $W_{\mathrm{in}} = 4$, $W_{\mathrm{ds}} = 4.5$ and $W_{\mathrm{nl}} = 5$ obtained from guess and test. While the exact reasons justifying the introduction of those factors are not known, they somehow rely on the challenge for a 1-D model to represent 2-D interactions.

Final WIM settings and parameters are shown in table 1.

TABLE 1: WIM settings and parameters.

Parameter	Symbol	Value
Gravitational acceleration	g	9.81 m s^{-2}
Sea water density	ρ_w	1025 kg m^{-3}
Grid spatial resolution	Δx	100 m
Time step	Δt	6.4 s
Number of frequency bins	n_f	36
Number of angular bins	n_θ	24
Lower frequency limit	$f_{\min}$	0.05 Hz
Upper frequency limit	$f_{\max}$	1 Hz
Weight for S_{in}	W_{in}	4
Weight for S_{ds}	W_{ds}	4.5
Weight for S_{nl}	W_{nl}	5

1.3 Results

1.3.1 Spectrum shape

Waves growing in the weighted WIM model are showing a power decay tail. The spectral shape as obtained at the end of each transect in open water is displayed in Figure 8 in both linear and logarithmic representation. From the peak toward the higher frequencies, the curves follow mostly a f^{-5} slope with an abrupt shift to a lower slope of f^{-4} in the middle frequencies, hence around 1.4 to 1.6 times the peak period f_p.

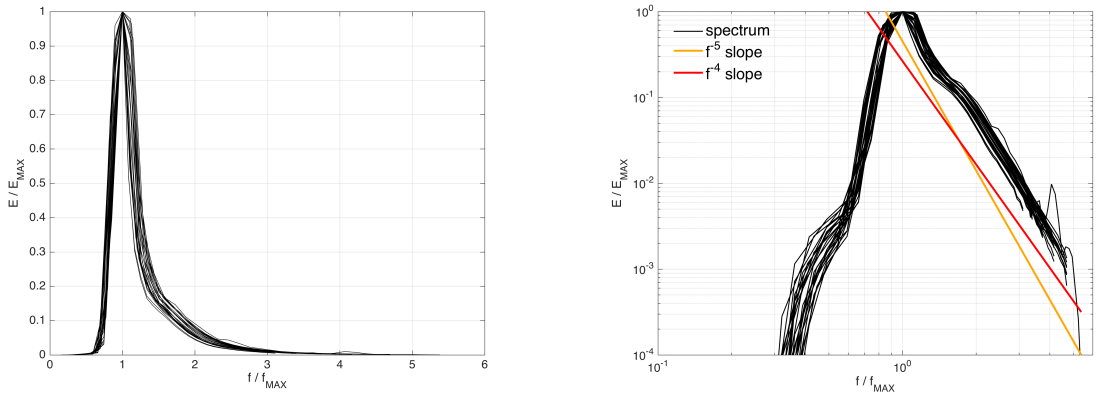

(a) Linear representation

(b) Logarithmic representation

FIGURE 8: Normalized shape of the spectrum at the end of each of the 25 selected transects in a linear (left) and logarithmic (right) scales. The red and orange lines correspond to f^{-4} and f^{-5} slopes.

1.3.2 Validation with WW3

As shown in Figure 9, a comparison between WIM and WW3 allowed to describe model results for H_s and T_p. From WW3, no peak period are found below 2 seconds. This is explained by the energy always persisting in the low frequencies as previously

shown (Fig. 7). Considering how WIM initial wave spectrum E_0 has been set, that is by generating a JONSWAP spectrum with energy (or H_s) associated to WW3 and ignoring T_p values, it was expected to have such differences for low peak period in WIM. Those low period values are thus corresponding to the initial growth of the wave spectrum occurring in the very first distance on which the spectrum is being advected. Thus, the T_p domain where results are not correlated for weak energy is contained by $T_p < 2.5$ s. Given by equation 1.21 for a JONSWAP spectrum, such peak period corresponds to a H_s of 25 cm. It suggests that WW3 waves with peak periods smaller than 2.5 seconds are too young so the still present energy in the low frequencies has not yet been transferred (by the wave-wave interactions) or overwhelmed by new energy entering the system, forced by the wind. This does not affect the total amount of energy though as shown with the comparative panel for H_s.

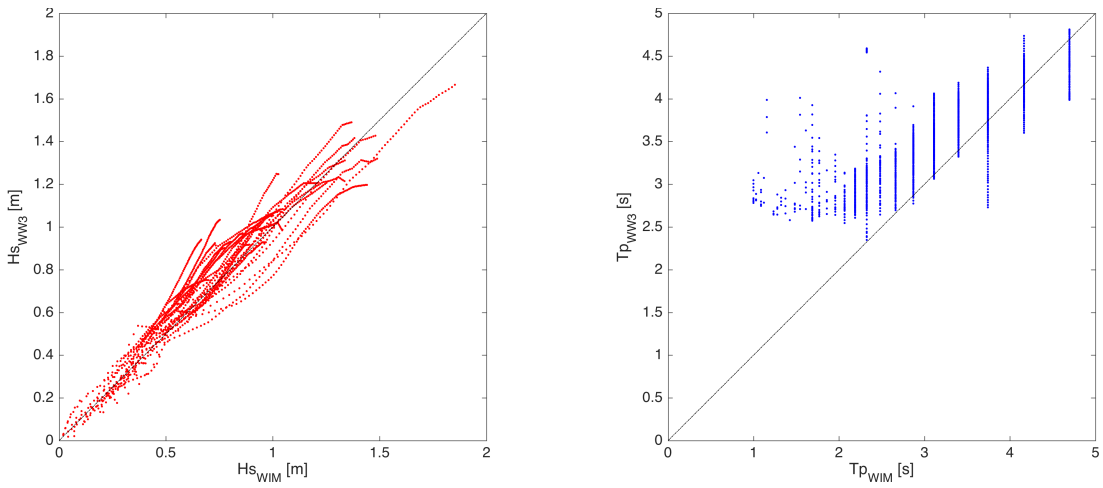

(a) H_s (b) T_p

FIGURE 9: Comparison between WIM and WW3 in terms of H_s (left) and T_p (right) for the 25 selected transects. Discretization in the T_p graphs is related to the limited number of frequency bins in the model.

For waves with peak periods higher than 2.5 seconds though, differences between the two models tend to decrease as T_p increases, meaning that the amount of energy in the lower frequencies gets important enough so the peak developing is now overwhel-

ming the initial energy distribution. Thus, this sets a limit where the comparison of T_p between WIM and WW3 is irrelevant.

To investigate results based on specific variables as position x or wind speed U_{10}, the normalized error NE (or relative difference) between models for a variable Y is, here, defined by

$$\mathrm{NE}_Y = \frac{Y_{\mathrm{WIM}} - Y_{\mathrm{WW3}}}{Y_{\mathrm{WW3}}} \tag{1.23}$$

and the root mean squared normalized error (RMSNE)

$$\mathrm{RMSNE}_Y = \sqrt{\frac{\sum(\mathrm{NE}_Y)^2}{N_x}} \tag{1.24}$$

has been evaluated for wave parameters $Y = Y(x)$, hence corresponding to $H_s(x)$ or $T_p(x)$ for the N_x transect grid points. The results are displayed in Figure 10. Based on the distance x, values for $7 \leq x < 40$ km show an overall NE slightly under zero but relatively constant for both H_s and T_p. Values for $x < 7$ km however, which are related to small waves, show a large, but rapidly decreasing (in amplitude), standard deviation. This is mostly a consequence of the previous results (Fig. 9) related to differences in initial wave configurations between models and, thus, variability expected with the young waves. Values for $x > 40$ km, however, show discontinuities due to the fact that the number of transects covering those distances is decreasing. Based on the wind velocity U_{10}, RMSNE values are decreasing for both H_s and T_p when wind is stronger. Data dispersion is globally higher for H_s than T_p but maximum RMSNE of near 30% is seen for T_p values corresponding to low U_{10}.

The normalized difference between WIM and WW3 as a function of both wind velocity U_{10} and position x are shown in Figure 11. The 3D representation shows the normalized error $\mathrm{NE}(x, U_{10})$ defined as a function of both variables. From those values, parametric least square plane has been calculated showing the overall trend considering

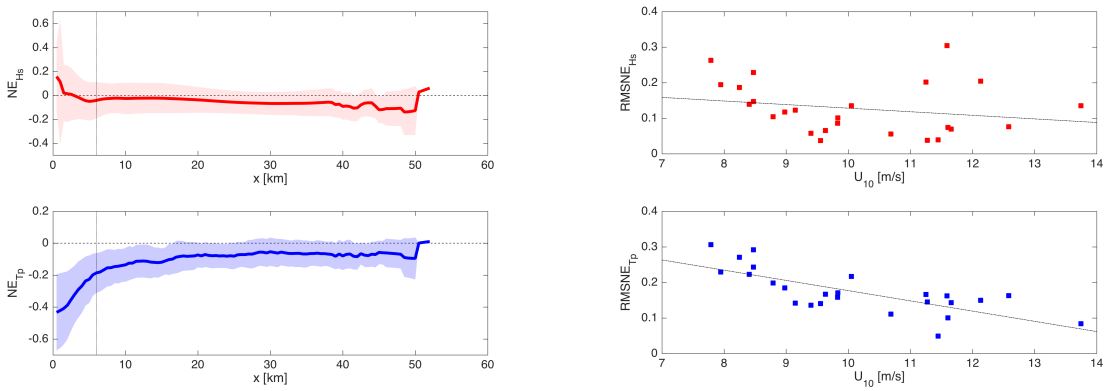

(a) NE(x) (b) RMSNE(U_{10})

FIGURE 10: General overview of the error between models by considering one variable at the time. The left panel shows the NE between WIM and WW3. The standard deviations are defined by the limits of the shaded area. The right panel shows the RMSNE between models for every transect as a function of the wind velocity. Red lines and markers are related to H_s and blue ones to T_p.

both parameters. According to previous results, data such that $x < 7$ km have been ignored in either the representation and the plane construction so focus was rather put on the part of the results where comparison between WIM and WW3 was relevant. This perspective presents the overall domain where WIM generally underestimates waves.

1.3.3 Wave-wave source term contribution

Results with and without nonlinear source term are represented in Figure 12. It clearly shows the importance of the wave-wave exchanges to shift the energy (from higher to lower frequencies) and allows the spectrum to evolve realistically. Not considering those interactions leads to a steady-state condition after a few kilometers. More specifically, setting $S_{nl} = 0$ has limited wave growth to a peak period below 2 s and significant height under 0.5 m, except for two transects. The exception is concerning the two transects with the highest initial energy, that not only do not gain energy but

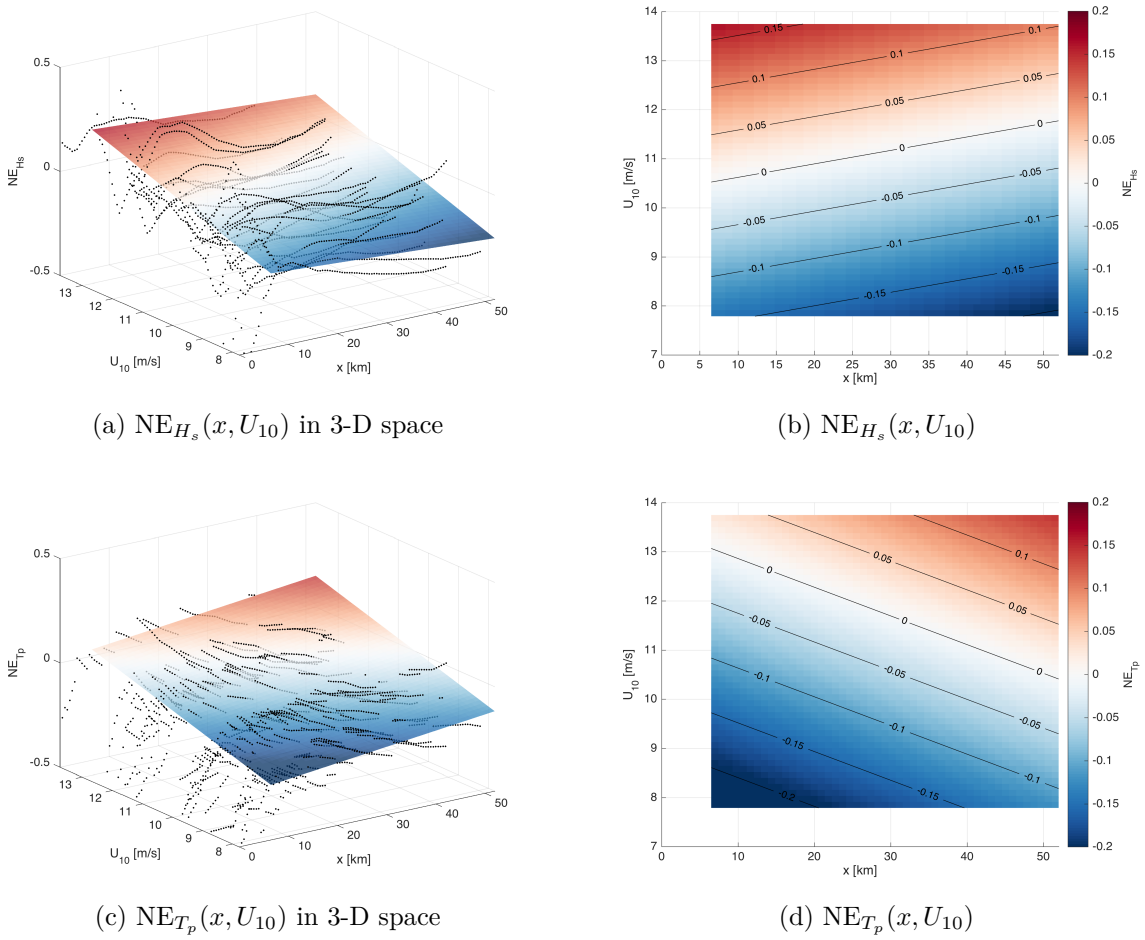

(a) $\mathrm{NE}_{H_s}(x, U_{10})$ in 3-D space

(b) $\mathrm{NE}_{H_s}(x, U_{10})$

(c) $\mathrm{NE}_{T_p}(x, U_{10})$ in 3-D space

(d) $\mathrm{NE}_{T_p}(x, U_{10})$

FIGURE 11: Normalized error (NE) between WIM and WW3 models. Model wave outputs from WW3 have been subtracted from WIM results and then divided by WW3 corresponding wave parameters H_s or T_p.

lose some. The gaps where T_p breaks toward lower values though are corresponding to the energy transferred from atmosphere to ocean and increasing until the peak newly formed gets more important than the initial peak from the lower frequencies. Along most transects, wave energy is increasing in both configurations but the peaks do not move toward lower frequencies without the nonlinear source term.

The overall underestimation when not considering S_{nl} term is so that wave growth goes to only 46% for Hs and 52% for T_p of the equivalent values including wave-wave

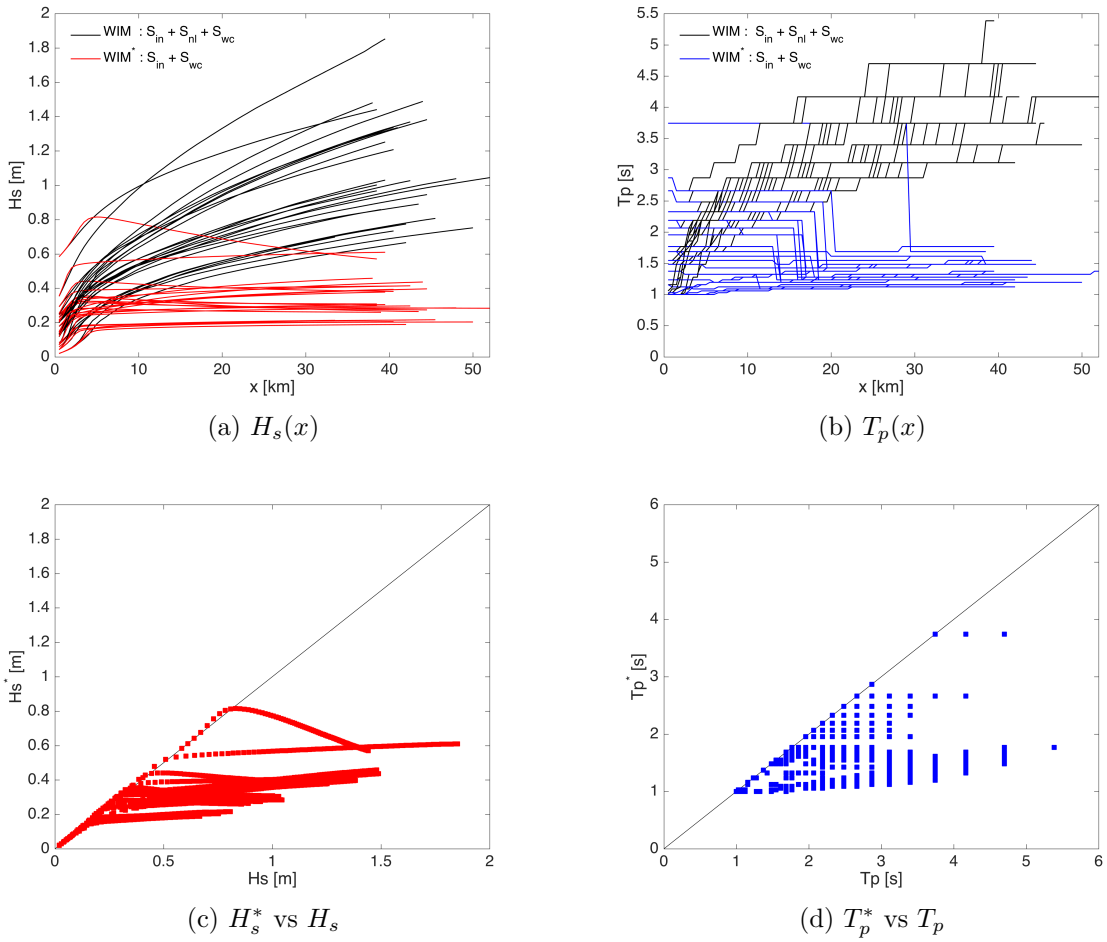

(a) $H_s(x)$ (b) $T_p(x)$

(c) H_s^* vs H_s (d) T_p^* vs T_p

FIGURE 12: WIM wave parameters with (H_s and T_p) and without (H_s^* and T_p^*) wave-wave interactions. The upper panels show the values along the 25 transects while the lower panel show the comparisons between models. Black lines represent runs with all three source terms. Red markers and lines are related to H_s and the blue ones to T_p.

interactions. Those values decrease respectively to 30% and 34% when taking into account only the last spatial bins of the transects. As shown in figure 13, trend is relatively constant for different wind velocities, especially when focusing on the spectrum resulting at the end of every transects. The variability is higher when considering the whole outputs. As previously shown in figures 9 and 10, this is explained by the larger difference in models when energy is low at the beginning of the transect. Thus this can be summarized by a general trend where neglecting nonlinear wave-wave interactions

leads to an underestimation of both Hs and Tp reaching approximately 30% after a few kilometers in a fetch-limited region.

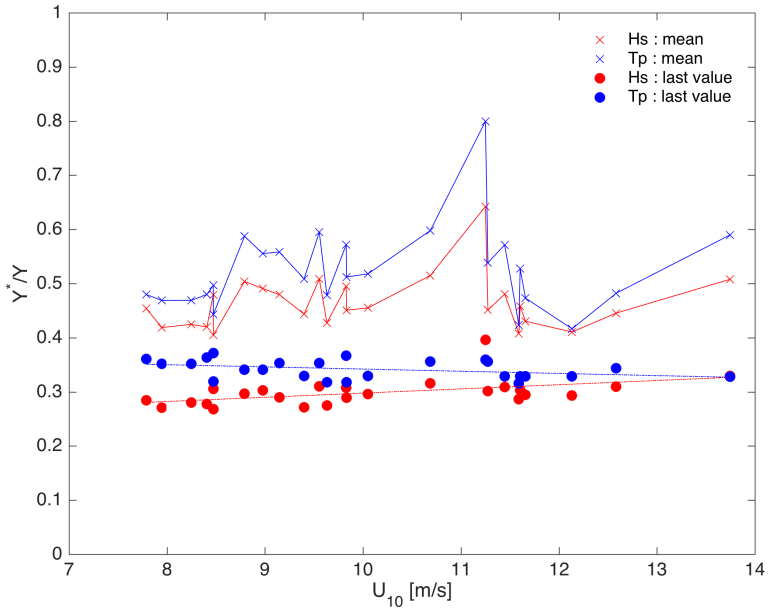

FIGURE 13: Relative comparison (Y^*/Y) between results obtained with and without S_{nl} terms for $Y = H_s$ or $Y = T_p$, Y^* being the runs done without nonlinear wave-wave interactions. The lines represent the mean value for each transect and the markers the value corresponding to the last spatial values of the N transects. The red and blue colors are referring respectively to the H_s and T_p parameters.

1.4 Discussion

Calibration of the new WIM version in open water has required weight coefficients to balance source terms to achieve good comparisons with WW3. The exact explanation or physical implications for the use of those coefficients is still to clarify. The challenge of integrating the nonlinear source term involving a 2-D spectrum along a 1-D spatial domain is expected to play a significant role but numerical configuration of the model may also be involved.

The determination of weight coefficients W_i has been done considering the three source terms S_{in}, S_{ds} and S_{nl}. It follows that using the same weight coefficients to evaluate only the first two may be biased. In that perspective, comparing WIM results with and without S_{nl} may appear inconsistent. But many different settings have been tested for $S_{\text{nl}} = 0$ and all of them resulted in a lack of energy and a peak period that could not migrate toward the lower frequencies at a certain point. Thus, the actual setting to evaluate the contribution of the nonlinear wave-wave interaction may rely on a certain choice but still appears to provide a realistic estimate of a fetch-limited wave spectrum growth. This addition of weights also implied to further overlook the nonlinear wave-wave interactions in this WIM version under ice cover considering that balance between S_{nl} was done considering both S_{in} and S_{ds}, but not S_{ice}. Therefore, resulting approximation of the energy balance equation (Eqs. 1.1 and 1.22) in WIM should rather be evaluated by

$$\frac{1}{c_g} D_t E = (1 - A)(W_{\text{in}} S_{\text{in}} + W_{\text{ds}} S_{\text{ds}} + W_{\text{nl}} S_{\text{nl}}) + A S_{\text{ice}}. \tag{1.25}$$

Not considering S_{nl} under the ice remains a realistic approximation (Cheng et al., 2017) considering that energy attenuation by the ice is 3-4 order of magnitude higher than the nonlinear wave-wave interactions (Dumont et al., 2020) and thus preferring equation 1.25 relies mostly on mathematical coherence than operational needs.

The model successfully reproduced the growth of a wave spectrum along transects for different wind velocities ranging from 8 to 14 m/s. Moreover, based on the 3G wave model features, which do not restrain the spectrum to a specific shape, WIM source terms have the capability to shift the peak frequency of the initial wave spectrum. This is very important in the foreseen perspective of integrating ice mechanisms such as attenuation where energy is much more impacted for the higher frequencies. While a wind bias is generally observed, no correction is applied at this stage.

Moreover, the calculation time required from WIM to run along a transect about

50 kilometers long and caracterized by a fine spatial resolution of 100 meters was under 60 seconds on a 8 Go MacBook Air (1,4 GHz Intel Core i5). This fast approach based on wind velocity only allows to investigate mechanisms intervening in the MIZ with a very simple model.

1.5 Conclusion

The new version of WIM has been developed to allow an initial spectrum shape to evolve with realistic H_s and T_p when compared to WW3 in open water for the fetch-limited conditions of the St. Lawrence Estuary.

The need of considering the nonlinear wave-wave interactions in WIM has been clearly highlighted. This conservative mechanism is essential to allow the frequency peak to move toward lower frequencies. Such role is central not only in the establishment of a wave spectrum but also in the foreseeing perspective of studying the evolution of such spectrum under an ice cover. While no energy is gained or loss, but only exchanged, the redistribution impacts the overall shape of the spectrum and, consequently, the input and dissipation source terms S_{in} and S_{wc}.

When many ice models used to study waves-ice interactions focus on mechanisms where ice cover is complete and thus directly force a wave spectrum at the ice edge, the perspective of using this new WIM version under a partial ice cover may be relevant considering the relatively large and scattered surface of ocean open to energy exchange between atmosphere and ocean. It may allow wave growth before reaching the ice edge and through polynyas. The present chapter has described the calibration and validation of the model considering the transfers of energy between the atmosphere and ocean. Next step would be to compare WIM with field data. Another step would be to validate and calibrate ice attenuation parametrization so ice distribution may be included along transects.

BIBLIOGRAPHIE

Bismuth, E., 2014. Interactions vagues-glace dans l'estuaire et le golfe du Saint-Laurent. Mémoire de maîtrise, Université du Québec à Rimouski, 96 p.

Booij, N., Haagsma, I., Holthuijsen, L., Kieftenburg, A., Ris, R., van der Westhuysen, A., Zijlema, M., 2006. SWAN Technical Documentation. Delft University of Technology. The Netherlands.

Cavaleri, L., Rizzoli, P. M., 1981. Wind wave prediction in shallow water : Theory and applications. Journal of Geophysical Research : Oceans 86 (C11), 10961–10973.

Cheng, S., Rogers, W. E., Thomson, J., Smith, M., Doble, M. J., Persson, O. P. G., Iii, C. O. C., Wadhams, P., Kohout, A. L., Ackley, S. F., Montiel, F., Shen, H. H., 2017. Calibrating a Viscoelastic Sea Ice Model for Wave Propagation in the Arctic Fall Marginal Ice Zone. Journal of Geophysical Research : Oceans 122, 8770–8793.

Collins, C. O., Rogers, W. E., Marchenko, A., Babanin, A. V., 2015. In situ measurements of an energetic wave event in the Arctic marginal ice zone. Geophysical Research Letters 42, 1863–1870.

Doble, M. J., De Carolis, G., Meylan, M. H., Bidlot, J.-R., Wadhams, P., 2015. Relating wave attenuation to pancake ice thickness, using field measurements and model results. Geophysical Research Letters 42, 4473–4481.

Dumont, D., Baudry, J., Sutherland, P., Barst, L., 2020. Constraining wave dissipation and non-linear interactions in the marginal ice zone Poster session presented at : Ocean Sciences Meeting, 16-21 February, San Diego, USA.

Dumont, D., Kohout, A., Bertino, L., 2011. A wave based model for the marginal ice zone including a floe breaking parameterization. Journal of Geophysical Research 116 (C04001), 1–12.

Goda, Y., 1988. Statistical variability of sea state parameters as a function of wave spectrum. Coastal Engineering in Japan 31 (1), 39–52.

Goda, Y., 1999. A Comparative Review on the Functional Forms of Directional Wave Spectrum. Coastal Engineering Journal 41 (1), 1–20.

Goda, Y., Suzuki, Y., 1975. Computation of refraction and diffraction of sea waves with Mitsuyasu's directional spectrum. Technical Note, Port and Harbour Research Institue 230, 45 p.

Hasselmann, K., 1962. On the non-linear energy transfer in a gravity-wave spectrum part 1. general theory. Journal of Fluid Mechanics 12 (4), 481–500.

Hasselmann, K., Barnett, T. P., Bouws, E., Carlson, H., Cartwright, D. E., Enke, K., Ewing, J. A., Gienapp, H., Hasselmann, D. E., Kruseman, P., Meerburg, A., Müller, P., Olbers, D. J., Richter, K., Sell, W., Walder, H., 1973. Measurements of Wind-Wave Growth and Swell Decay during the Joint North Sea Wave Project (JONSWAP).

Hasselmann, S., Hasselmann, K., 1985. Computations and Parameterizations of the Nonlinear Energy Transfer in a Gravity-Wave Spectrum. Part I : A New Method for Efficient Computations of the Exact Nonlinear Transfer Integral. Journal of Physical Oceanography 15 (11), 1369–1377.

Hasselmann, S., Hasselmann, K., Allender, J. H., Barnett, T. P., 1985. Computations and Parameterizations of the Nonlinear Energy Transfer in a Gravity-Wave Specturm. Part II : Parameterizations of the Nonlinear Energy Transfer for Application in Wave Models. Journal of Physical Oceanography 15 (11), 1378–1391.

Holthuijsen, L. H., 2007. Waves in Oceanic and Coastal Waters. Cambridge University Press, Campbridge.

J Saucier, F., Roy, F., Gilbert, D., Pellerin, P., Ritchie, H., 2003. Modeling the formation and circulation processes of water masses and sea ice in the Gulf of St . Lawrence , Canada. Journal of Geophysical Research 108 (C8), 1–20.

Komen, G. J., Hasselmann, S., Hasselmann, K., 1984. On the Existence of a Fully Developed Wind-Sea Spectrum. American Meteorological Society 14, 1271–1295.

Meylan, M. H., Bennetts, L. G., Kohout, A. L., 2014. In situ measurements and analysis of ocean waves in the Antarctic marginal ice zone. Geophysical Research Letters 41, 5046–5051.

Miles, J. W., 1957. On the generation of surface waves by shear flows. Journal of Fluid Mechanics 3 (2), 185–204.

Mitsuyasu, H., Tasai, F., Suhara, T., Mizuno, S., Ohkusu, M., Honda, T., Rikiishi, K., 1975. Observations of the Directional Spectrum of Ocean Waves Using a Cloverleaf Buoy 5, 750–760.

Neumeier, U., Ruest, B., Lambert, A., Bismuth, E., Dumont, D., Jacob, D., Savard, J.-P., Joly, S., 2013. Modélisation du régime des vagues du golfe et de l'estuaire du Saint-Laurent pour l'adaptation des infrastructures côtières aux changements climatiques (rapport final présenté au ministère des Transports du Québec). Tech. rep.

Resio, D. T., Perrie, W., 2008. A two-scale approximation for efficient representation of nonlinear energy transfers in a wind wave spectrum. Journal of Physical Oceanography 38, 1–37.

Ruest, B., Neumeier, U., Dumont, D., Bismuth, E., Senneville, S., Caveen, J., 2016. Recent wave climate and expected future changes in the seasonally ice-infested waters of the Gulf of St. Lawrence, Canada. Climate Dynamics 46 (1), 449–466.

Smith, G. C., Roy, F., Brasnett, B., 2013. Evaluation of an operational ice – ocean analysis and forecasting system for the Gulf of St Lawrence. Royal Meteorological Society 139 (January 2013 B), 419–433.

Snyder, R. L., Dobson, F. W., Elliott, J. A., Long, R. B., 1981. Array measurements of atmospheric pressure fluctuations above surface gravity waves. Journal of Fluid Mechanics 102, 1–59.

Tang, C. L., Yao, T., Perrie, W., B M, D., Toulany, B., Dunlap, E., Wu, Y., 2008. BIO Ice-Ocean and Wave Forecasting Models and Systems for Eastern Canadian Waters. Tech. Rep. 261.

The WAMDI group, 1988. The WAM Model - A Third Generation Ocean Wave Prediction Model. American Meteorological Society 18, 1775–1810.

Tolman, H. L., 1992. Effects of numerics on the physics in a third-generation wind-wave model. Journal of Physical Oceanography 22 (10), 1095–1111.

Tolman, H. L., 2009. User manual and system documentation of WAVEWATCH-IIITM version 3.14. User manual and system documentation of WAVEWATCH III version 3.14 (3.14), 220.

Tolman, H. L., Banner, M. L., Kaihatu, J. M., 2013. The NOPP operational wave model improvement project. Ocean Modelling 70, 2–10.

Tolman, H. L., Krasnopolsky, V. M., 2004. Nonlinear interactions in practical wind wave models. In : 8Th International Workshop on Wave Hindcasting and Forecasting. Maryland, USA, p. 15 p.

van Vledder, G. P., 2012. Efficient algorithms for non-linear four-wave interactions. In : ECMWF workshop on Ocean Waves. Reading (England), pp. 97–112.

Wadhams, P., Squire, V. A., Goodman, D. J., Cowan, A. M., Moore, S. C., 1988. The attenuation rates of ocean waves in the marginal ice zone. Journal of Geophysical Research : Oceans 93 (C6), 6799–6818.

Williams, T. D., Bennetts, L. G., Squire, V. A., Dumont, D., Bertino, L., 2013a. Wave – ice interactions in the marginal ice zone . Part 1 : Theoretical foundations. Ocean Modelling 71, 81–91.

Williams, T. D., Bennetts, L. G., Squire, V. A., Dumont, D., Bertino, L., 2013b. Wave – ice interactions in the marginal ice zone . Part 2 : Numerical implementation and sensitivity studies along 1D transects of the ocean surface. Ocean Modelling 71, 92–101.

WMO, 1998. Guide to Wave Analysis and Forecasting. World Meteorological Organization.

Wu, J., 1982. Wind-stress coefficients over sea surface from breeze to hurricane. Journal of Geophysical Research : Oceans 87 (C12), 9704–9706.

Young ;, I. R., van Vledder, G. P., 1993. A Review of the Central Role of Nonlinear Interactions in Wind-Wave Evolution. The Royal Society publishing 342 (1666), 505–524.

CHAPITRE II

STUDY OF WAVE-ICE INTERACTIONS IN THE ST. LAWRENCE ESTUARY USING SAR IMAGERY AND WAVE MODELING

Abstract

Wind fields from the Canadian Regional Deterministic Prediction System (RDPS) have been used with Sentinel-1 SAR images covering the St.Lawrence Estuary for winters 2016 to 2019 to estimate the wave and ice patterns. Transects with partial ice covers under wind stress have been extracted from 3 selected images and waves predicted using the 1-D Wave-in-Ice-Model (WIM). The resulting wave spectra evolving along those transects allowed to characterize ice distribution impact on wave significant height and peak period. The impact of ice distribution was also parameterized in term of effective fetch for those specific cases. Results have been compared with in-situ observations showing large biases but opening new avenues for further investigation.

2.1 Introduction

Observation of the sea surface by satellite-borne sensors has significantly enhanced the modelling of the sea state and highlighted problems as the role of the surface gravity waves interfering with the ice cover and shaping the marginal ice zone (MIZ) (Williams et al., 2013). Moreover, measurements on which are based the actual models or parametrizations to study those mechanisms are spaced by many kilometers or even more (Wadhams et al., 1988; Squire and Moore, 1980; Wadhams et al., 1988; Liu et al., 1991). Even recent studies (Meylan et al., 2014; Doble et al., 2015) are based on buoys deployed about 50 km apart. Those distances do not allow to describe interactions

intervening between atmosphere, ice and ocean at smaller scales. However, interactions at small scale may lead to some feedback that may have impacts on much larger scales (Williams et al., 2013). Local fragmentation of the ice cover, for example, relies on energy attenuation and may lead to increase the fetch which impacts the wave growth.

This study is motivated by the qualitative and quantitative description of waves-ice interactions based on observations. This includes in-situ wave data, operational model forcing datasets and satellite imagery. Focus is put on the specific ice distribution found in the St. Lawrence Estuary where ice cover is seasonal, thus discontinuous and very variable in space and time. In the perspective to synthesize results, an attempt is done here to express wave growth in term of fetch which is an important variable for wave growth in coastal systems (Mason et al., 2018).

First section describe some theoretical about the SAR imagery which have been used to describe ice distribution. Second section describes the parametrization implemented into Wave-in-Ice Model (WIM) to evaluate the attenuation by the ice. Third section describes data used to characterize specific scenes and the study cases resulting. Wave spectrum travelling into those study cases are analyzed in the fourth section. Discussion about the perspectives, challenges and limitations of the method is presented in the fifth section.

2.1.1 Remote sensing SAR imagery

Synthetic Aperture Radar (SAR) is a high-resolution remote sensing system widely used for Earth observation and monitoring since more than 30 years. The system can be mounted on an airborne or spaceborne platform and provides unique imaging capability by its independence to daylight or clouds coverage. Now more than 20 spaceborne SAR systems are being actually operated (Moreira et al., 2013) and products are, for instance, used to evaluate ice cover and extent, iceberg movements or estimate

best ship routes. While pixel-level ice classification is not possible (Lee et al., 1994), large area of ice are widely classified by trained analysts to provide coarse ice maps (Ochilov and Clausi, 2010).

SAR imaging is based on electromagnetic micro waves pulses, few centimeters wavelength, that are transmitted and backscattered. The amplitude and the phase of the echo depends on the physical and electrical properties of the surface, thus the roughness and the permittivity with different polarizations that allow to focus on specific properties of the surface. Roughness may be influenced by wind or waves, slick, current or ice. The carrying platform, aeroborne or spaceborne, moves so the relative location of the antenna to the target changes with time. The successive recorded echoes combined with the multiple antenna positions forms the synthetic antenna aperture and allow a much higher resolution than an equivalent static antenna. Swath generally varies from 20 km to 500 km.

2.1.2 Canadian ice charts

The Canadian Ice Service (CIS) is using SAR images for mapping ice coverage and stage of evolution over navigable waters in Canadian waters. Ice analysts provide daily ice charts for the arctic ocean and for the St. Lawrence but the products of those analyses consist in large scale polygons where high resolution feature analysis is not possible (Figure 14). According to the World Meteorological Organization (WMO) standard for ice type and concentration, the ice age and form and up to three types for a single region is given. into a classification table named as the egg code referring to his oval shape. No segmentation or classification is done inside a polygon though. This consequently provides a continuous, in time and space, set of ice data. However, considering the daily basis of the interpretations, such representation may show some limitation in the attempt to describe the ice distribution in a specific time during the day.

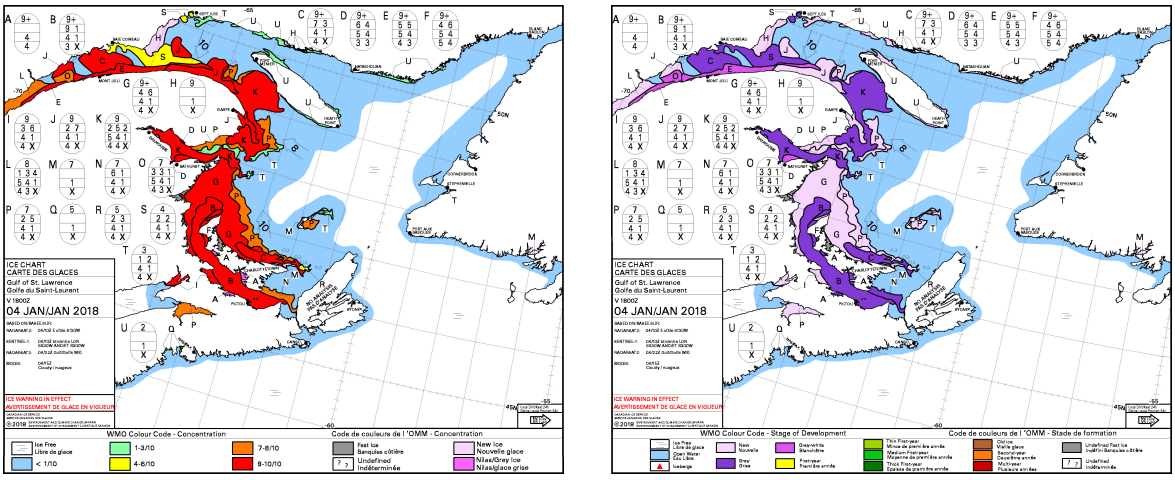

(a) Ice concentration (b) Stage of development

FIGURE 14: Ice charts provided by the CIS for the Gulf of St. Lawrence showing ice concentration (left) and stage of development (right). The egg code contains the ice data up to three specific types of ice for a region.

From the CIS ice charts, climatology (Figure 15) for years 1997 to 2019 shows that ice in the lower St. Lawrence estuary (LSLE) starts appearing during early December while the concentration peaks during the first two weeks of February. Then ice concentration decreases so the LSLE is clear of ice near the end of March. This leads to a high variability of ice conditions in the LSLE over approximately four months (Figure 16).

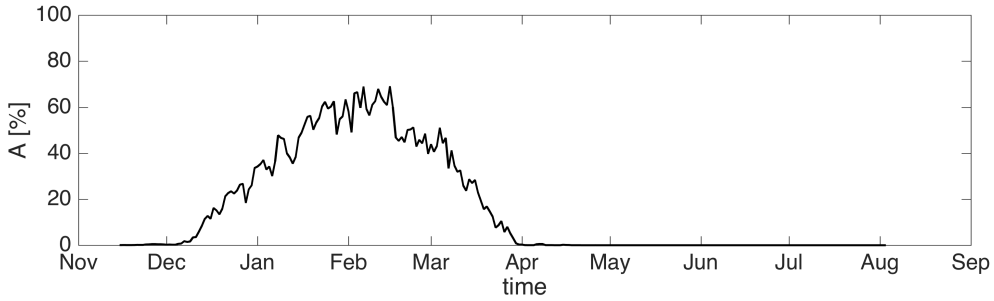

FIGURE 15: Seasonal climatology for the daily mean ice concentration over the LSLE based on the CIS ice charts from 1997 to 2019.

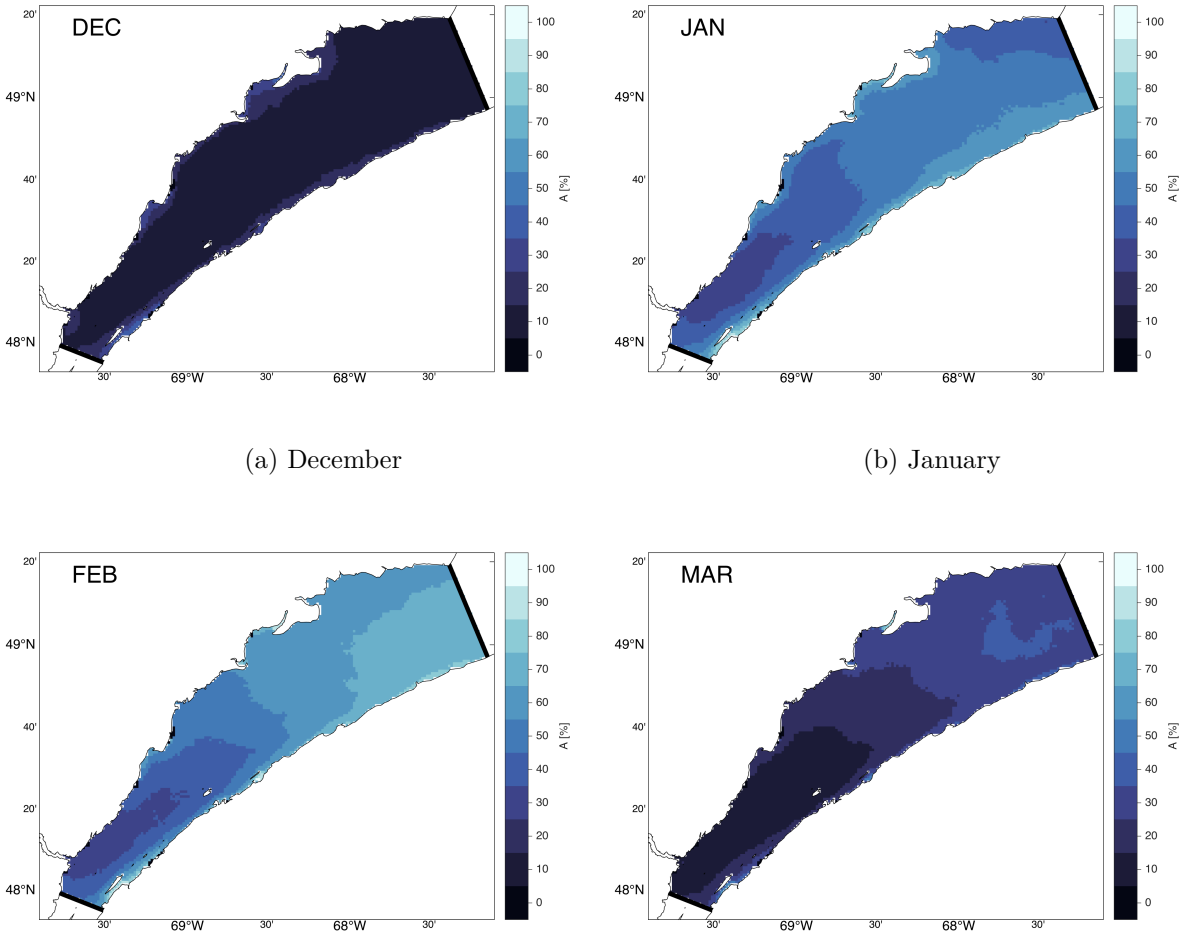

(a) December

(b) January

(c) February

(d) March

FIGURE 16: Monthly mean ice concentration for the LSLE during December, January, February and March based on the CIS ice charts from 1997 to 2019. The concentration increases from dark to light colors.

2.2 Ice attenuation parameterization

The attenuation of the waves by the ice can be represented by a source term S_{ice} which is based on a exponential decay of energy, hence

$$S_{\text{ice}}(f) = -\alpha E(f) \tag{2.1}$$

where E is the wave spectrum and α the rate of energy loss due to the ice. To evaluate the ice attenuation coefficient α, the model from Sutherland et al. (2018) was implemented into Wave-in-Ice Model (WIM) described in Chapter 1.

While many models assume the ice to be vertically homogeneous, ice may vary and be represented by more than one layer. Temperature gradient, possible presence of bulk salinity or variable ice density are examples of factors impacting ice column variability. The parameterization used here consider a two-layer structure. As shown in Figure 17, the lower layer formed by a mix of ice and water is assumed to be viscous and allows wave motion (oscillating pressure gradient) while the upper layer is assumed to be impermeable and does not permit such motion. The relative proportion of those two layers is given by $\epsilon \in [0, 1]$ such that ϵh is the thickness of the bottom layer. Consequently, it can be tuned towards different types of ice and the wavenumber-dependent decay rate is

$$\alpha(k) = \epsilon \Delta_0 h k^2. \tag{2.2}$$

The parameter $\Delta_0 \in [0, 1]$ gives the boundary condition at the bottom of the ice. $\Delta_0 = 1$ implies a no-slip condition and corresponds to the upper bound for ice dissipation. It has been suggested by Ardhuin et al. (2018) that the relation between ice distribution and Δ_0 is related to the ratio between wavelength and floe size and that weakening the no-slip condition according to an empirical formulation may improve

model results. However, it is not clear what physical process is implied and thus Δ_0 remains difficult to evaluate.

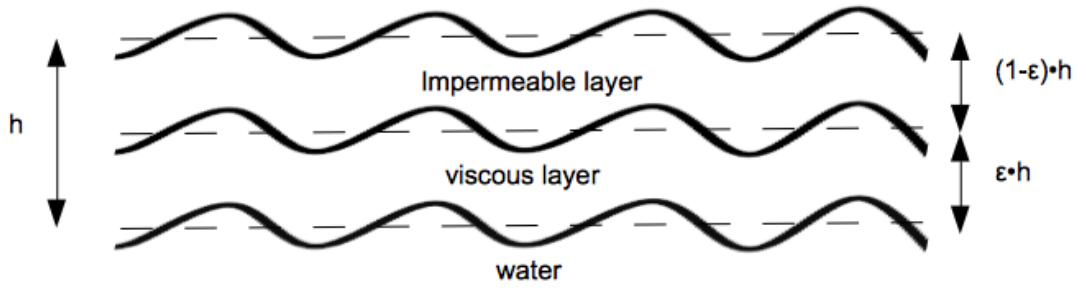

FIGURE 17: Illustration of the two-layer model used in WIM. The figure has been modified from Sutherland et al. (2018).

The determination of parameter ϵ is also a challenge to evaluate since it relies on the structure of the ice at a very fine scale. Here, ice is assumed to be horizontally homogeneous. For practical purpose, the value of ϵ and Δ_0 have been taken together and set so $\epsilon\Delta_0 = 0.5$. This estimation has been done according to previous experiments made on wave data collected in the Parc national du Bic during BicWin mission (Dumont et al., 2020). Thus, the implemented α coefficient for ice attenuation is

$$\alpha(k) = 0.5hk^2 \tag{2.3}$$

where $k = \omega^2/g$ is the wave number and h is the ice thickness.

2.3 Datasets and Methodology

2.3.1 Ice distribution from SAR imagery

Satellite SAR image data were acquired from Sentinel-1A, which is the first of five missions from the European Space Agency (ESA) and aims to produce a consistent long

term data imaging for land and ocean services. The constellation is composed of two polar-orbiting satellites running in a cycle of 12 days with a 180° orbital phase difference. The resulting repeat cycle is 6 days. The pair collects microwave pulse measurements sent to the Earth and back to the satellite at a frequency of 5.405 GHz (C-band). Data is delivered under 24 hours and available from winter 2015.

Images acquisition mode is interferometric wide swath (IW) with a swath range of 250 km. Radar frequency is 5.405 GHz and spatial resolution is 10 m. The images used were acquired from December 2015 to March 2019 over the St. Lawrence estuary. The whole dataset consists of 32 level-1 ground range detected (GRD) SAR images. Both VV and VH polarizations have been visualized but only VV was kept for analysis since it was providing more ice details. Images metadata is displayed in the Annex A.

The raw images were cropped into smaller spatial domains corresponding to LSLE. A range-Doppler terrain correction was applied before to reproject them into a WGS84 coordinates system. The canadian coastline (2011) from Statistic Canada was superposed to images to ensure accurate segmentation with coast and islands.

2.3.2 Scenes selection

The model is forced by hourly CMC Regional Deterministic Prediction System (RDPS) with horizontal resolution of 10 km which was interpolated on the 5 km oceanic model resolution (Smith et al., 2013). The wind field was superposed over the LSLE to evaluate wind pattern attributed to each image. Temporal (linear) interpolation was done to match the sensing time of SAR images and temporal analysis was done for the previous hour to ensure wind stationarity (velocity and direction) in time. For further analysis, selected images were those with unidirectional and strong cross-shore wind. Waves are assumed here to be generated by wind only. This assumption is done according to the presence of ice that attenuates waves generated elsewhere and the shape

of the LSLE Ice concentration generally increases toward the Gulf of St. Lawrence where fetch usually gets larger when there is no ice coverage.

Images with complete ice cover were discarded as well as images with no ice. So, images selected as region of interest (ROI) were those with strong unidirectional wind blowing cross-shore toward an AWAC location with a clear segmentation of ice and water. Figure 18 shows the distribution of the images based on those environmental criteria. From the initial 32 SAR images, only 9 fit those general criteria. Image description according to those criteria is displayed in Annex B. When looking at the specific ice distribution however, 6 of them were rejected because the ice was concentrated on a specific area rather than being somehow organized into ice bands (or patches) offshore the AWAC locations. So only 3 images were finally kept as ROI.

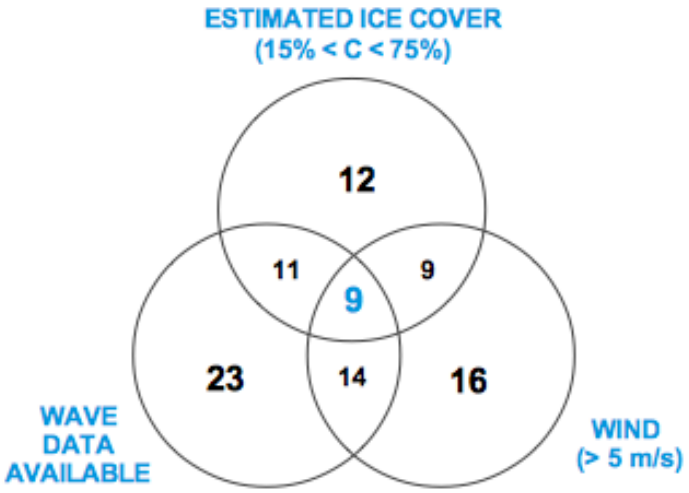

FIGURE 18: Categorization of the 32 SAR images according to the three general environmental criteria. Numerical values are for number of images fitting those criteria. From those criteria only 3 images were finally kept as ROI based on the specific ice distribution

2.3.3 Wave field data acquisition

Wave data were acquired from two Nortek 1-MHz AWAC-AST (acoustic wave and current profiler) deployed in the St. Lawrence Estuary. Measurements were done hourly for 17 minutes at a frequency of 2 Hz. One of the AWAC was located offshore the Baie du Ha ! Ha ! (48.3465°N, 68.8518°W) in the Bic national park during winter 2018 (December 1, 2017 to April 25, 2018) and the other alongside Pointe-à-Boivert (48.6591°N, 69.0441°W), near Forestville during winter 2017 (November 14, 2016 to April 23, 2017).

2.3.4 Transect extraction from SAR images

For every ROI images, a theoretical transect was created to fit the wind trajectory toward the AWAC. As shown in Figures 19, 20 and 21, segmentation was done along transects by the creation of ice polygons based on SAR images texture.

Because (ice or water) attribution of every pixel is impossible, classification needs to be interpreted according to the neighborhood (Ochilov and Clausi, 2012). Among modern techniques to classify ice texture, many include co-occurrence probabilities where many statistical values are weight together and attributed to an ice class (Clausi, 2001). To achieve such classification, knowledge of the class statistic is needed and algorithms have to be calibrated and validated based on local images (Clausi, 2001; Scott et al., 2015) which could not be done for the actual study. Here, ice concentration (A) for every patch (or polygon) was determined based on the single pixels energy distribution, which is considered to be the best classification statistical feature for texture analysis of SAR sea ice imagery when considering only one feature (Soh and Tsatsoulis, 1999). A color threshold τ was set based on the brightness distribution to classify pixels p_i,

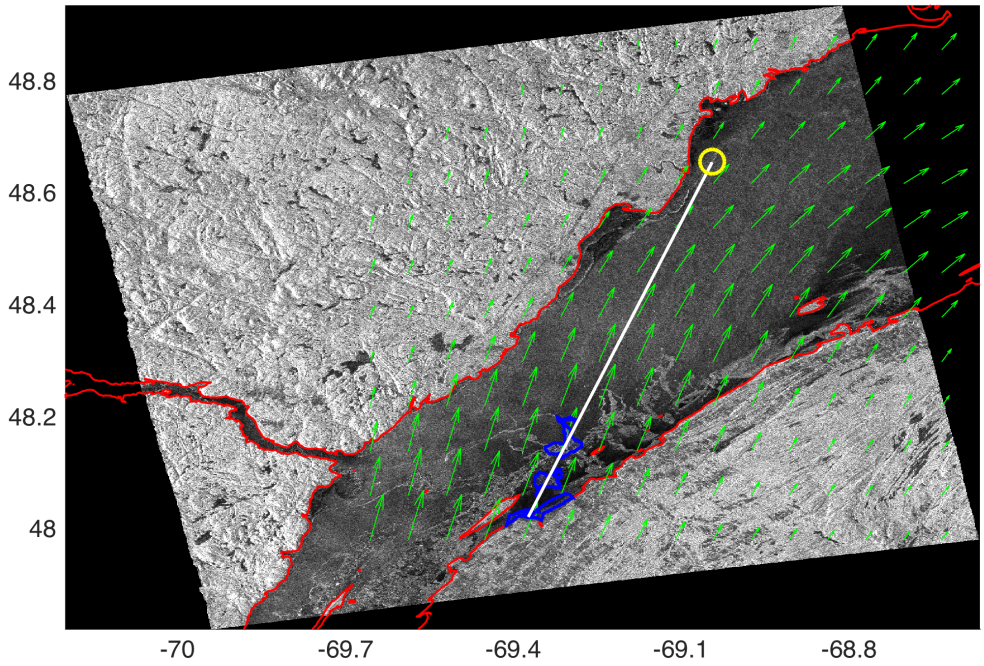

FIGURE 19: Scene of 9 January 2017 (SC1). The white line is the transect and the wind field is represented by green arrows. The ice region around the transect is delimited by the blue polygon and the yellow mark is the location of the AWAC offshore Forestville.

either as ice or water as follow :

$$P_i = \{p_i | P(p_i) \geq \tau\}, \tag{2.4}$$

$$P_w = \{p_i | P(p_i) < \tau\}. \tag{2.5}$$

The method allowed to set thresholds so the resulting binary classifications were visually matching the original SAR images (Figure 22). No downsampling was done of the SAR images or polygons nor any filter applied to smooth speckles.

Since no observation data allowed to set specific values, a constant ice thickness

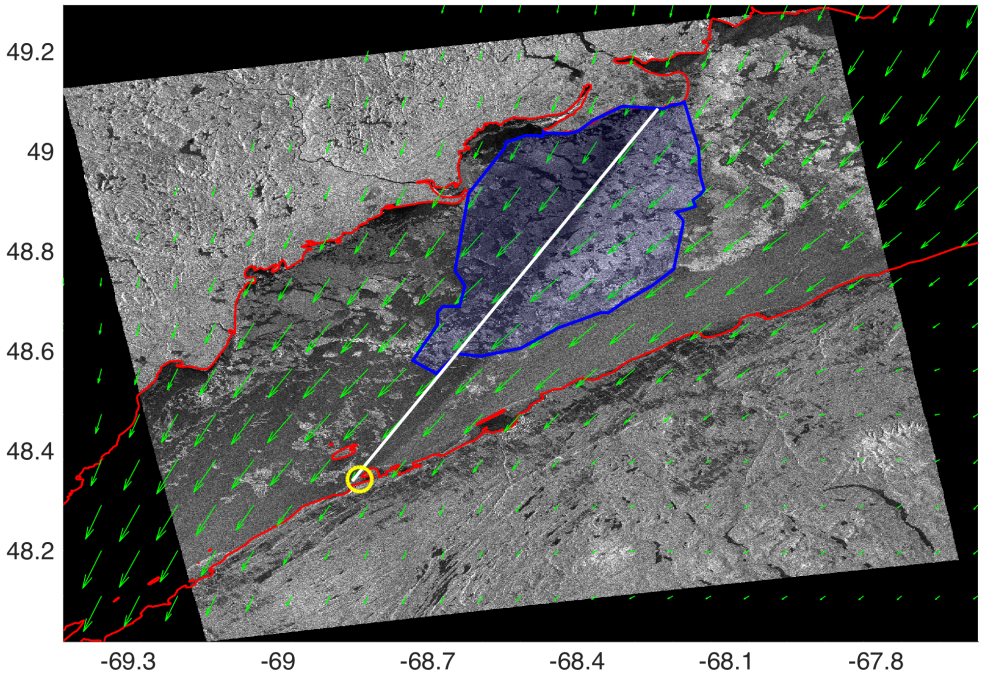

FIGURE 20: Scene of 4 January 2018 (SC2). The white line is the transect and the wind field is represented by the green arrows. The ice region around the transect is delimited by the blue polygon and the yellow mark is the localization of the AWAC offshore the Baie du Ha ! Ha !.

h has been determined for each polygon along transect based on CIS ice charts (see Annex C) but modulated with the contextual scene analysis considering that charts were daily and covering large spatial areas.

According to the visual assessment of ice polygons, an uncertainty ϵ_A has been attributed to the concentration. A thickness uncertainty ϵ_h has been chosen large to cover likely scenarios based on CIS ice charts local variability (in space and time) over the LSLE. Those uncertainties were kept as data and used in the later modelling to set limits for the model results.

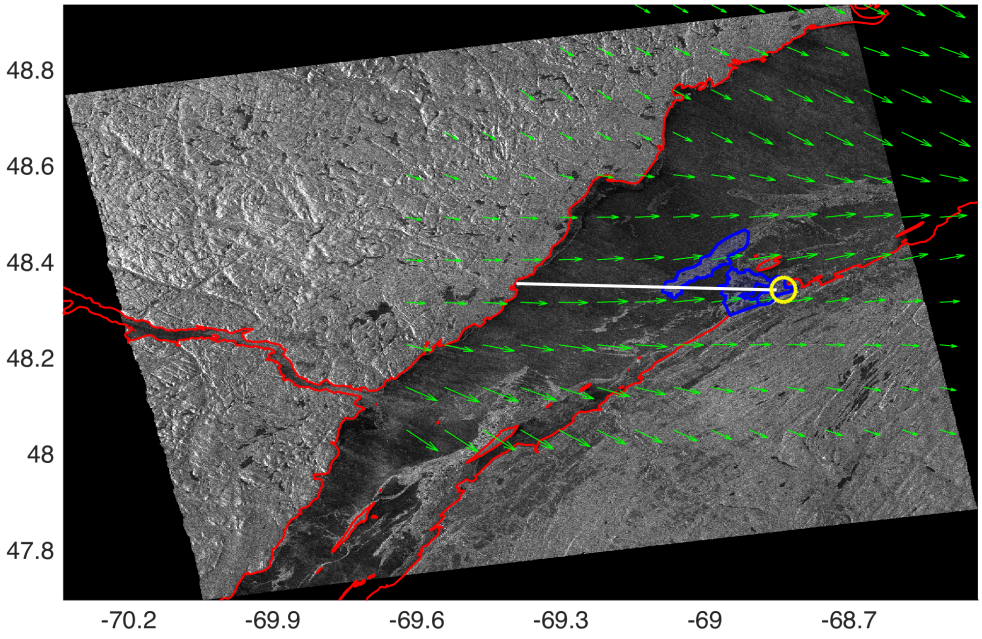

FIGURE 21: Scene of 28 January 2018 (SC3). The white line is the transect and the wind field is represented by the green arrows. The ice region around the transect is delimited by the blue polygon and the yellow mark is the localization of the AWAC offshore the Baie du Ha ! Ha !.

2.3.5 Resulting study cases

The first study case (SC1) corresponds to 9 January 2017 where the LSLE is mostly free of ice except along the south shore where ice bands a few kilometers wide are present. The wind is blowing toward NE at 12 m s^{-1}. The second study case (SC2) happened on 4 January 2018 during a strong wind event. The northern side of the LSLE is mostly covered by ice while a region nearly 10 km wide and free of ice is present along the south shore. The wind is blowing toward SW at 13 m s^{-1}. The third study case

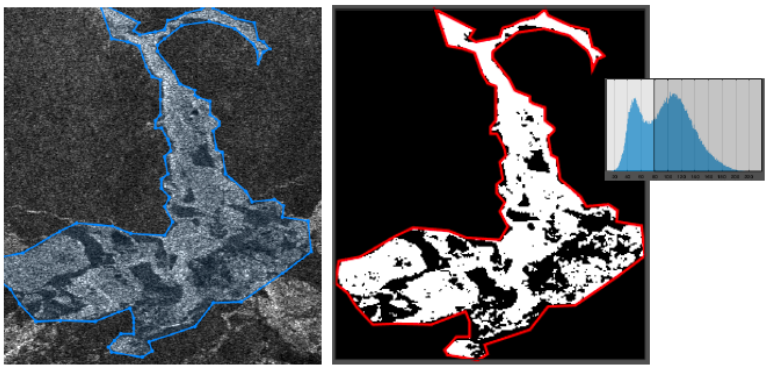

FIGURE 22: Ice classification example (from SC1) based on pixels color. Histogram shows the pixel brightness distribution. Left image is the polygon defined after the SAR image while right image is the resulting classification (ice is white).

(SC3) corresponds to 28 January 2018 where the wind is blowing toward E at 6 m s^{-1}. The northern side of the LSLE is free of ice but the south side is characterized by long ice bands and ice packs.

2.3.6 Wave-in-Ice-Model (WIM) setup

The Wave-in-Ice model (WIM) described in Chapter 1 was run with ice parameters and forcing extracted from each of the three study cases (SC). Based on the WIM calibration process where non-null energy spectrum was input to trigger wave growth, a low energy JONSWAP spectrum was prescribed as input in the SC, here corresponding to $H_s = 2.5$ cm. The spatial grid resolution was 100 m. Constant wind value along transect was given by previous characterization of the SC. For every SC, WIM was run with different ice distributions to evaluate sensitivity to uncertainty. A basic transect with no ice $\mathrm{ICE_{NO}}$ was given as reference. Then considering ϵ_A and ϵ_h uncertainty or local variability about ice parameters A and h, runs with maximal ice volume $\{A_{\max}, h_{\max}\}$ and minimal ice volume $\{A_{\min}, h_{\min}\}$ were also calculated. Table 2 summarizes those ice configurations which led to describe every SC in terms of corresponding H_s

and T_p.

TABLE 2: Ice conditions for WIM runs prescribed for each case study.

Runs	Concentration	Thickness
ICE_0	A	h
ICE_{NO}	0	0
ICE_{MIN}	$A - \epsilon_A$	$h - \epsilon_h$
ICE_{MAX}	$A + \epsilon_A$	$h + \epsilon_h$

Moreover, sensitivity evaluation within ice patches have been analyzed by creating 25 different ice distribution where ice feature A and h were set randomly inside the variability domain ($A \pm \varepsilon_A$) and ($h \pm \varepsilon_h$). Mean concentration and mean thickness within each ice polygon were left equal to previous estimates to allow only local variations. Those transects are later described by ICE^*.

No uncertainty have been attributed when $A = 0$.

2.3.7 Effective fetch

From previous results, wave spectrum growth have been converted into an effective fetch to summarize waves condition according to the ice distribution. Such representation has been used by Ruest et al. (2016) in the Gulf of St. Lawrence to evaluate the wave climate with the consideration of the attenuation by sea ice.

Basically, $H_s^*(x)$ is the significant wave height for a case with no ice. Hence, H_s^* is a continuous monotonic increasing function in the present context where offshore waves are wind generated from an initial flat water surface. Thus, it can be reversed so $f = x(H_s^*)$ where f is the fetch corresponding to the distance over which the wind is blowing in its main direction. Such relation also applies to T_p. Ice cover is attenuating wave energy, thus resulting effective fetch depends on the ice spatial distribution,

concentration and thickness. The effective fetch is defined here as

$$f_e^{Hs}(x) := f(Hs(x)) \tag{2.6}$$

$$f_e^{Tp}(x) := f(Tp(x)) \tag{2.7}$$

which consequently describes the fetch that would have yielded an equivalent wave spectrum if there was no ice along the transect.

2.4 Results

2.4.1 1-D scenes representation

Conversion from SAR scenes to a one dimensional representation is shown in Figure 23. Visual segmentation allowed to identify polygonal ice regions while classification of every polygons was done by both combined analytic and contextual interpretation as previously described.

2.4.2 Wave growth along transects

Figure 24 shows the evolution of H_s and T_p along SC1, SC2 and SC3 transects. Reference curves are also drawn, which show H_s and T_p growth for corresponding transects without ice. The presence of ice rapidly decreases H_s, hence the total wave energy, while T_p abruptly shifts toward higher periods. Transitions from the ice to open water allow both energy and peak period to increase, but after abruptly shifting down for the second one.

Results for the three cases show rapid peak period increasing under ice cover which represents the migration of the peak due to the attenuation of the high frequencies energy rather than the input of some new energy in the spectrum. The first 60 km in

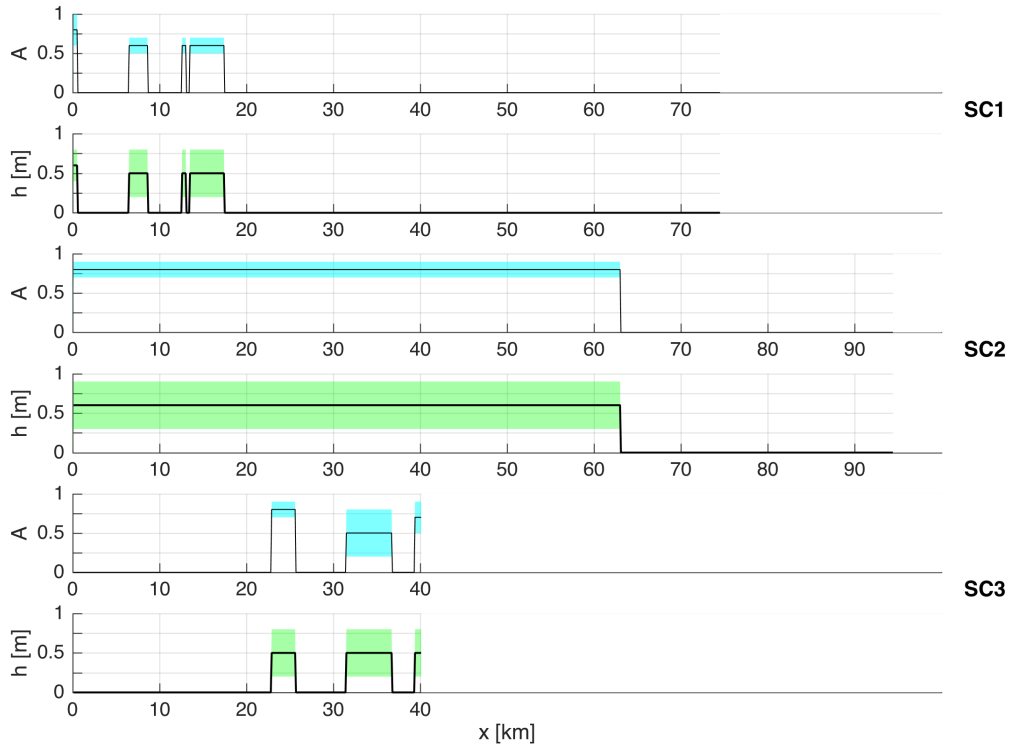

FIGURE 23: Ice characterization (concentration A and thickness h) for each transect. Upper two panels are for SC1, middle ones for SC2 and bottom ones for SC3. Blue and green shadings areas show the uncertainties for ice parameters C and h.

SC2 where energy is almost null and peak period close to or over 8 seconds highlights that peak period, by itself, does not distinguish substantial waves from small attenuated waves since both have large Tp. Thus when considering only one parameter, H_s may appear as a better indicator of the state of the wave spectrum than T_p. In both SC1 and SC2, transition from ice cover to open water shows a fast energy gain before the growth slows down. This is not seen in SC3 where wind speed is the lowest with only 6 m s^{-1} and total H_s never reach over 0.5 m. This may suggest minimum wind velocity threshold might be needed for such transition.

As seen in SC1 and SC2, cases without ice allow more energy to be injected in the

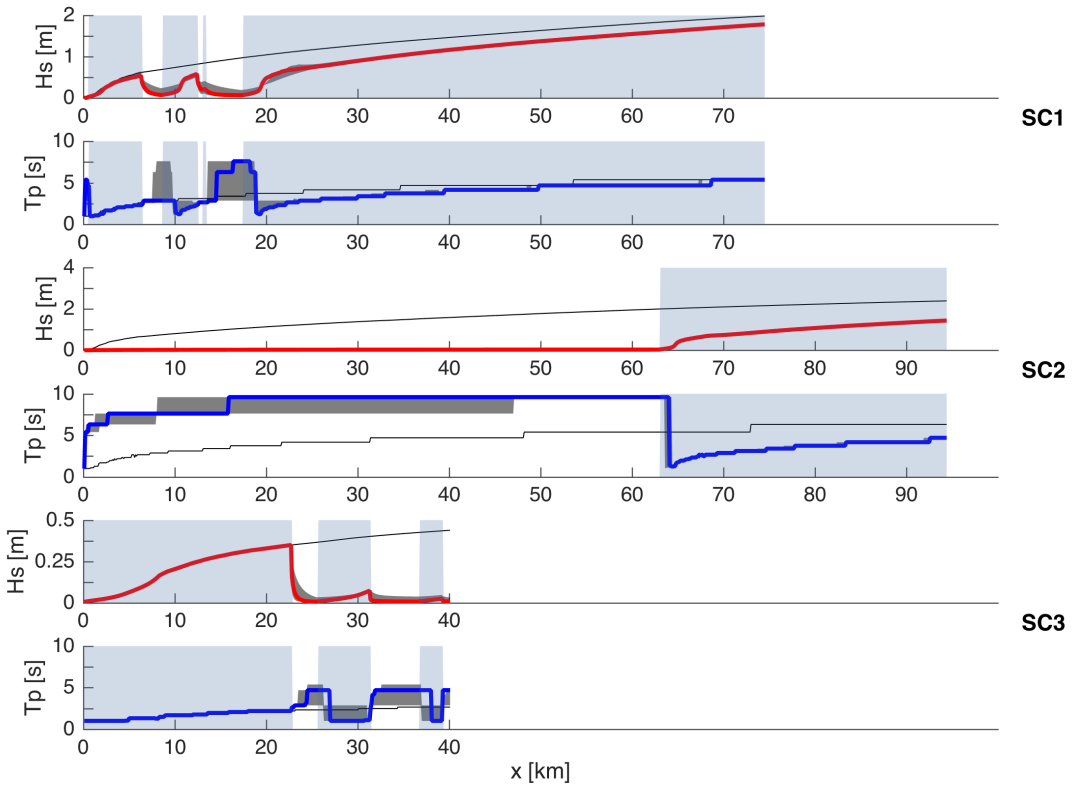

FIGURE 24: Evolution of wave parameters along transects SC1 (top panels), SC2 (middle panels) and SC3 (bottom panels). Red lines are for H_s and blue lines for T_p with $\mathrm{ICE_{MIN}}$ and $\mathrm{ICE_{MAX}}$ results bordered by the dark grey shadings. Blue and white backgrounds show the water or ice presence along transects independently of C and h. Black lines are for the reference ice-free conditions (ICE_{NO}).

waves and resulting H_s is higher than with ice presence. While ice attenuates energy, the gain in the open water sections leads the spectrum to grow in a way that $H_s(x)$ tends to approach the corresponding iceless values with increasing distance. The same convergence seems to characterize T_p suggesting that if ice affects the wave spectrum locally, the following open water region – if sufficiently large – may then allow the spectrum to reshape in a form ressembling that in the absence of ice cover. When considering $\{A_{\min}, h_{\min}\}$ or $\{A_{\max}, h_{\max}\}$ as displayed by grey shaded areas, both H_s and T_p show some variability. For H_s, those variations are mainly localized under ice covers,

while for T_p, it extends on the open water areas following ice covers. This variability is further discussed in the next section.

2.4.3 Impact of ice variability

Figure 25 shows the ice parameters sensitivity within the uncertainty domain attributed to every ice patches. It shows the WIM outputs for H_s growth for previously described ICE runs (Table 2) and suggests that extremum ice values withing the attributed variability only slightly impact total wave energy.

Bottom panels display the normalized error

$$\mathrm{NE}^*_{HS} = \frac{H^*_s - H_s}{H_s} \tag{2.8}$$

where $H^*_x(x)$ is the WIM outputs obtained for the ICE^* transects with variable concentrations and thicknesses within ice patches. Emphasis is put on the comparative display between extreme cases ($\mathrm{ICE_{MIN}}$ and $\mathrm{ICE_{MAX}}$) for minimum and maximum ice covers and ICE^* where ice features were randomly distributed inside the uncertainty domain.

Intersections of wave growth curves for $\mathrm{ICE_0}$, $\mathrm{ICE_{MIN}}$ and $\mathrm{ICE_{MAX}}$ runs suggest that wave growth is sensitive not only to the total energy but to the spectrum shape. Nonlinear transfer may affect the redistribution of the energy within frequencies, thus accelerate gain or loss of energy on the short term. Those effects however are very local since they seem to intervene mostly during the closely-spaced transitions of ice and water in SC1, and these effects tend to disappear within a few kilometers of open water.

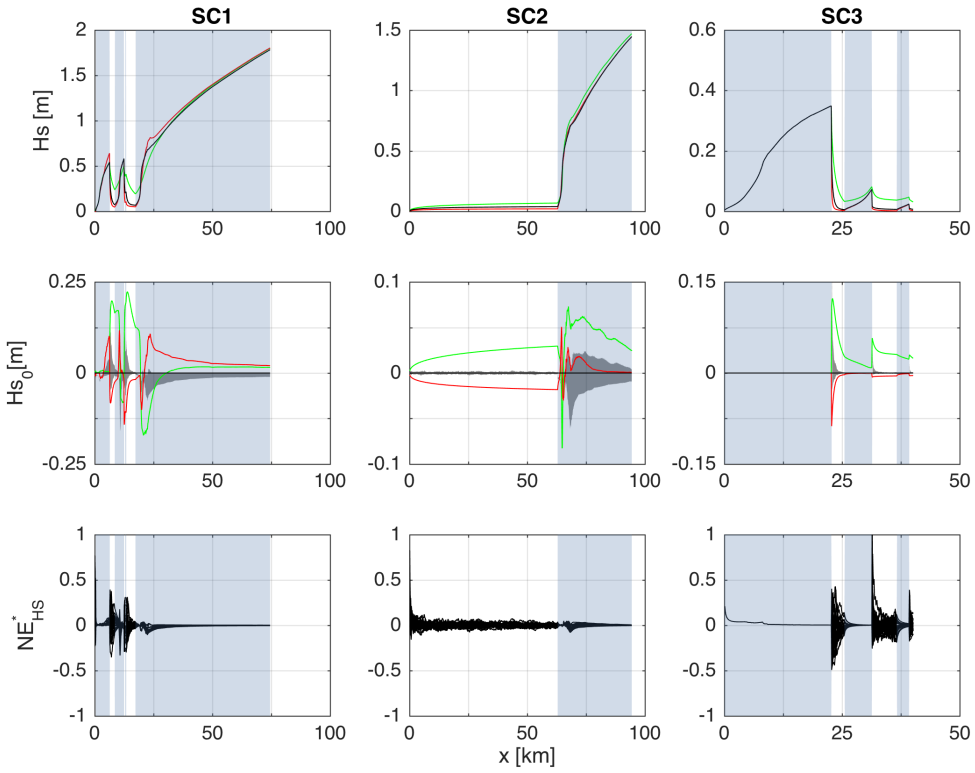

FIGURE 25: Impact of the ice variability on SC transects. Columns from left to right are for SC1 to SC3. The blue shaded areas are ice-free while white backgrounds represent iced regions with no distinction for concentration. Upper panels show ICE_0 (black), $\mathrm{ICE}_{\mathrm{MIN}}$ (green) and $\mathrm{ICE}_{\mathrm{MAX}}$ (red) model runs and middle panels show the differences of those runs with ICE_0. Bottom panels show the NE^*_{HS} for the ICE^* runs whose limits are also represented in the middle panels as grey shaded areas.

2.4.4 Ice distribution impact on effective fetch

Figure 26 shows the effective fetch for the three SC. For effective fetch expressed in term of T_p, values that were superior to maximal T_p^0 or inferior to minimal T_p^0 given by the reference ice-free scenarios, were ignored. The proportion of those rejected values is 6, 65 and 28% for study cases 1, 2 and 3. This suggests that fetch defined from H_s is more consistent for analysis and likely more applicable in future studies.

The conditions leading to spurious T_p values are related to either a wave spectrum with little energy or the rapid transition between water and ice. The first case is represented by SC2 where initial ice cover does not permit the waves to develop for a long distance but energy is not null in the low frequencies. This resulted in a situation where f_e^{Tp} is larger than the absolute fetch. The second case appears during transition from water to ice where wave energy is decaying but at a rate at which the peak does not move immediately. Thus, f_e^{Tp} changes are delayed from f_e^{Hs}. When considering only $f_e^{H_s}$, ice presence leads to a rapid decrease of the effective fetch, which becomes almost null within a few hundred meters for our cases. The following ice-free area leads to a linearly increasing effective fetch with $\Delta f_e/\Delta x \approx 1$ in the three cases. Consequently, at the LSLE scale, ice distribution affects the f_e decay rate but does not affect the following increasing rate when energy is transferred again from the atmosphere to the wave spectrum.

Bottom panels highlight that $f_e^{H_s}$ was generally superior or equal to $f_e^{T_p}$ after removing all the values out of T_p^0 boundaries. Exceptions are found when wave energy is low either at the beginning of the transect during initial growth or just after an ice band or patch.

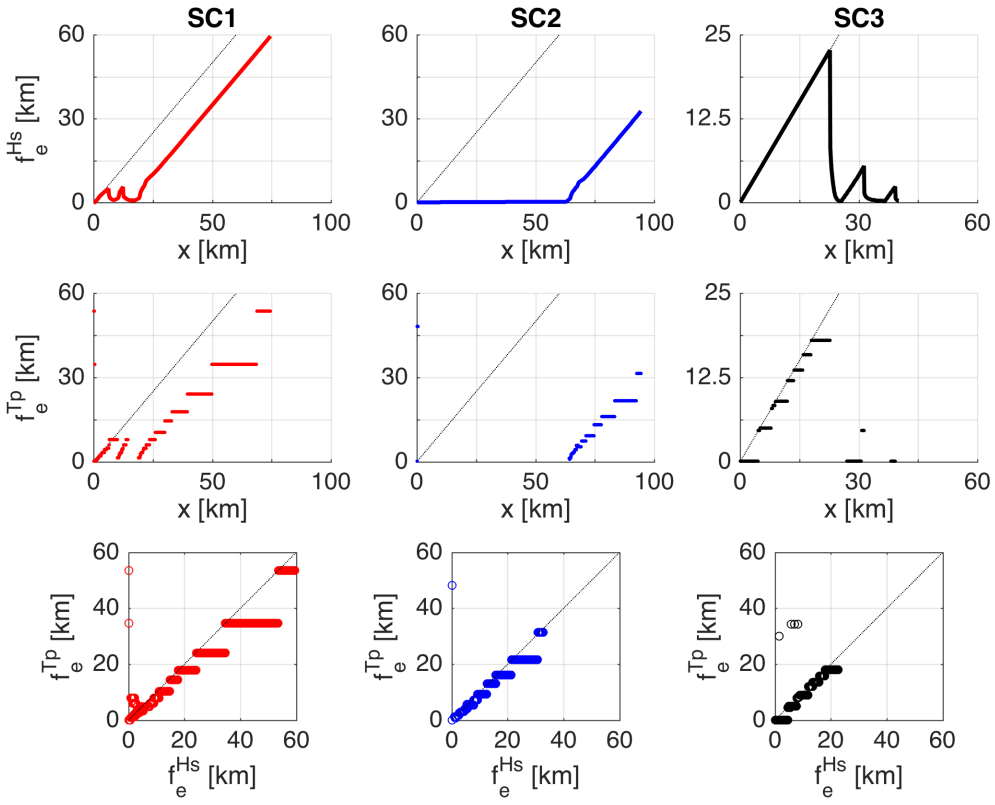

FIGURE 26: Effective fetch for the 3 study cases. Red,blue and black lines are respectively for SC1, SC2 and SC3 and grey lines show the $1:1$ ratio. Upper panels represent f_e^{Hs}, middle panels f_e^{Tp} and lower panels the scatterplots of f_e^{Hs} and f_e^{Tp}.

2.4.5 Model validation with field data

Table 3 synthesizes the SC information by displaying the wind velocity for each SC, the transect length and the wave parameters H_s and T_p obtained from an AWAC for the nearest period to the SAR images. Previous and following measurements are also shown, providing the short time trend. Validation was done by comparing WIM results with AWAC field data (Figure 27). No data was available for SC3 from the AWAC because of the ice cover over the instrument.

Even by considering the temporal variability of the wave parameter Hs and Tp

TABLE 3: Waves H_s and T_p field data (from AWACs) corresponding to each study case. Wind speed U_{10} (averaged along transect) comes from GEM model. Distance d is referring to the length of each transect. For every case, the AWAC location is corresponding to the last coordinates of each transect.

	H_s [cm]			T_p [s]			U_{10} [m/s]	d [km]
	21h20	22h20	23h20	21h20	22h20	23h20		
SC1	61	**66**	72	4.1	**4.9**	3.4	12.3	74.5
SC2	37	**76**	104	2.7	**3.3**	3.9	12.9	94
SC3	n/a	**n/a**	n/a	n/a	**n/a**	n/a	6	40

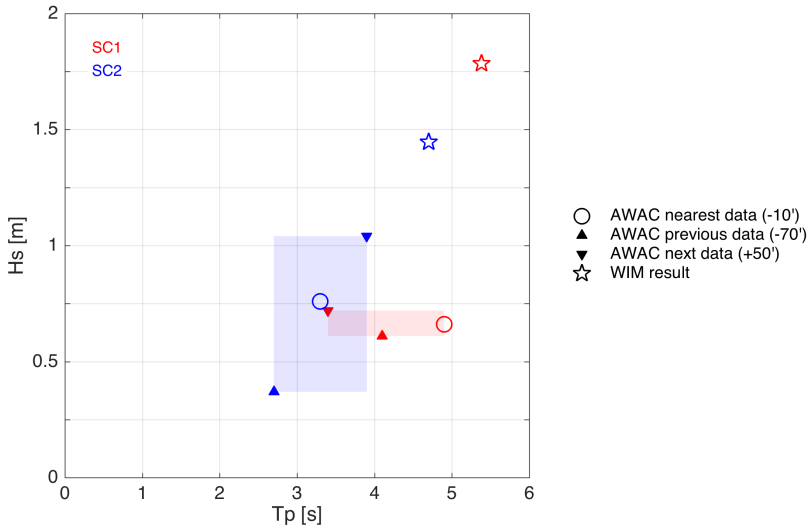

FIGURE 27: Comparison of the WIM wave results with AWAC data for every study cases. Red and blue colors are referring to study cases 1 and 2. The presence of ice over the AWAC location for the study case 3 led to an absence of waves. The star markers show results obtained with WIM. Circle markers are for the AWAC records during the SC while triangular ones are for previous and following records.

in the previous and following AWAC bursts, WIM failed to correctly predict the wave parameters. While no field data was available for SC3, corresponding Hs and Tp obtained with WIM for SC1 and SC2 are both exceeding field values. Respectively for Hs and Tp, outputs from WIM overestimated the AWAC values by a factor of 2.92 and

1.31 for SC1 and 1.90 and 1.42 for SC2. When compared with JONSWAP Hs/Tp ratio curve, results show that WIM energy is higher for a given peak period.

2.5 Discussion

2.5.1 Specific cases

In order to distinguish some theoretical and restrictive considerations from a more realistic, and thus, complex point of view, it appears relevant to point out some elements that might have played a role on energy flux within the wave spectrum and, thus, appears a challenge to be included in a further and more realistic study. Effects from the shore may have impacted wave spectrum growth through neglected mechanism (refraction, diffraction, bottom friction) as seen in SC1 and SC2 where transects ended close and parallel to the shore. More specifically, SC2 is related to an increasing storm which may have also led to stronger interferences from neighbouring regions that cannot be evaluated in WIM. Currents, while being known to affect the wave energy distribution, have also been neglected for simplicity.

Results from WIM show excess of energy in the final wave spectra. While it may be attributed to WIM conception or configuration, it may also be related to incapacity to identify some ice structures, since no validation has been done on SAR images. Moreover, only uncertainties for $A > 0$ has been taken into account which could lead to overestimate wave growth. This points out that the role of low ice concentration value may consequently have an impact but also the challenge to attribute features values based on images. A ground truth dataset for ice covering the LSLE could lead to more robust and automatic methods to segment and classify ice regions. Currently CIS ice experts are the reference for classification since no instrument covering large spatial domain can provided ice data.

Chapter 1 has shown a wind-speed dependent bias on the WIM results. This bias has been neglected at this point. Moreover, the wind input in WIM is set constant and evaluated over the whole transect while spatial variability exists. In a further step, a wind sensibility analysis could highlight the importance of the wind speed variability.

2.5.2 Method validity

Modelling 1-D transects through ice bands under constant wind stress in WIM has shown limits in the attempt to describe wave growth accurately. Uncertainties about the wind variability and the ice description were large and wind bias has been ignored. Nevertheless, results from WIM have shown over-estimation of both Hs and Tp for studied cases characterized with AWAC data. However, the short amount of data available makes it difficult to attribute the discrepancies obtained directly to the model. Other reasons may have contributed to such differences. One pillar on which WIM was built is that the wave field is supposed azimuthally symmetric and formed by local wind stress only. Thus no swell or any wave component from elsewhere is taken into account. This hypothesis may be applicable considering an ice cover relatively important in the neighbourhood that attenuates most of the waves travelling from elsewhere. Considering effects from the whole LSLE would impact energy spectrum by asymmetrically considering energy advection. Thus nonlinear wave-wave interactions might not be well represented which raises some questions about the applicability of such a 1-D model. Moreover, is there a minimum ice concentration value that is required to allow our method to be applicable ?

On a more specific analysis based on every SC, other elements might have impacted waves growth. According to the LSLE depth (and resulting large kH), waves were travelling in deep water. But SC1 and SC2 transects were ending only a few kilometers away from the shore. Boundary proximity (shore or bottom) might have locally impacted waves and contributed directly to energy transfers or indirectly, through nonlinear

wave-wave energy exchanges.

2.5.3 Data availability limitations

The process has highlighted some mandatory conditions to analyze waves-ice interactions based on imagery availability. First is the large amount of images needed, since lots of them may be expected not to fulfilled basic contextual conditions (ice cover, wave presence and wave measurements for the corresponding period). While all criteria may be fulfill in a single image to be considered as ROI, the probability of finding such ROI increases with the availability of the images. In that perspective, it appears fundamental to access more images to pursue with the method. In the forthcoming future where satellite-borne SAR imagery availability is expected to increase, this may facilitate the process. Secondly, defining SC and extracting transects of interest relies on very local ice and waves distributions and thus is related to measurement instruments location when needed to compared model predictions with observations. Consequently, there is a strong relation between the AWAC location and the potential transect orientations that may (or may not) worth to be considered.

Another fundamental aspect of the approach has been found in the LSLE ice distribution. Due to the polynia found at the head of the LSLE, the images have generally shown a western side of the LSLE less covered by ice than the eastern side. Some images had large variability on ice concentration leading to situations where ice was mostly located west of the AWAC location and east side of the study area was covered with very little ice. Moreover only a few images were showing clear ice bands. This heterogeneous, in time and space, ice distribution emphasize the relation between the number of locations with wave measurements and the probabilities of finding ideal ice distribution that can be studied. Since the method relies only on a fetch-limited region with available wave measurements and ice distribution, enlargement of the dataset could be obtained by a larger spatial cover of AWAC measurements.

2.6 Conclusion

From the daily CIS ice charts where ice regions are large polygons providing ice type and concentration, details on finer scales in space and time can be obtained by the direct analysis of SAR images. The low number of analyzed cases does not allow to generalize our results based on effective fetch. It only permits to suggest some applications for further investigation. The ice distribution in our SCs has resulted in attenuating most of the wave energy within a few hundred meters to a few kilometers depending on the ice concentration and thickness. The corresponding effective fetch was rapidly decreasing under the ice cover and then linearly increasing in the following open water regions. This shows that a short section of ice may have a strong impact on the wave energy spectrum and, consequently, knowing the ice distribution on a fine scale is important.

Characterizing ice distribution with SAR images has proven an excellent tool. However, in the perspective of studying waves-ice interaction many criteria had to be fulfilled in the selection of the images. From the initial 32 SAR images, only 3 were used, the rest having been discarded either because (1) there was no wind and consequently no waves, (2) there was no AWAC nor any field data available at the time of the image, or (3) there was no ice along any transect parallel to the wind and passing over field data. Thus the amount of images available and indirectly the source of those images appeared to a limiting factor. Transects matching the ice distribution, provided by SAR images, and oriented in the wind direction were input to WIM wave 1-D model. The resulting H_s and T_p along transect allowed to determine an effective fetch when compared to iceless equivalent transects. This single parameter characterization of the impact of ice distribution on waves condition could be used to summarize, on a larger scale, the wave climate.

Comparing field data from AWAC with WIM results has shown large differences

for both H_s and T_p and thus may suggest that WIM is not a pertinent tool to study waves-ice interactions in cases where ice coverage is partial. At the same time, very little image data were available which have restricted the comparison to only two cases. Accessing more images and consequently more related field data might give statistical weight to such conclusion.

BIBLIOGRAPHIE

Ardhuin, F., Boutin, G., Stopa, J., Girard-Ardhuin, F., Melsheimer, C., Thomson, J., Kohout, A., Doble, M., Wadhams, P., 2018. Wave Attenuation Through an Arctic Marginal Ice Zone on 12 October 2015 : 2 . Numerical Modeling of Waves and Associated Ice Breakup. Journal of Geophysical Research : Oceans 123 (8), 5652–5668.

Clausi, D. A., 2001. Comparison and fusion of co-occurrence , Gabor and MRF texture features for classification of SAR sea-ice imagery. Atmosphere-Ocean 39 (3), 183–194.

Doble, M. J., De Carolis, G., Meylan, M. H., Bidlot, J.-R., Wadhams, P., 2015. Relating wave attenuation to pancake ice thickness, using field measurements and model results. Geophysical Research Letters 42, 4473–4481.

Dumont, D., Baudry, J., Sutherland, P., Barst, L., 2020. Constraining wave dissipation and non-linear interactions in the marginal ice zone Poster session presented at : Ocean Sciences Meeting, 16-21 February, San Diego, USA.

Lee, J. S., Jurkevich, L., Dewaele, P., Wambacq, P., Oosterlinck, A., 1994. Speckle filtering of synthetic aperture radar images : A review. Remote Sensing Reviews 8 (4), 313–340.

Liu, A. K., Holt, B., Vachon, P. W., 1991. Wave propagation in the marginal ice zone : Model predictions and comparisons with buoy and synthetic aperture radar data. Journal of Geophysical Research : Oceans 96 (C3), 4605–4621.

Mason, L. A., Riseng, C. M., Layman, A. J., Jensen, R., 2018. Effective fetch and relative exposure index maps for the Laurentian Great Lakes. Sci Data 5 (180295), 1–7.

Meylan, M. H., Bennetts, L. G., Kohout, A. L., 2014. In situ measurements and analysis of ocean waves in the Antarctic marginal ice zone. Geophysical Research Letters 41, 5046–5051.

Moreira, A., Prats-iraola, P., Younis, M., Krieger, G., Hajnsek, I., Papathanassiou, K. P., 2013. A Tutorial on Synthetic Aperture Radar. IEEE Geoscience and Remote Sensing Magazine (march), 6–43.

Ochilov, S., Clausi, D. A., 2010. Automated Classification of Operational SAR Sea Ice Images. In : Canadian Conference Computer and Robot Vision. Waterloo, ON, Canada, pp. 40–46.

Ochilov, S., Clausi, D. A., 2012. Operational SAR Sea-Ice Image Classification. IEEE Transactions on Geoscience and Remote Sensing 50 (11), 4397 – 4408.

Ruest, B., Neumeier, U., Dumont, D., Bismuth, E., Senneville, S., Caveen, J., 2016. Recent wave climate and expected future changes in the seasonally ice-infested waters of the Gulf of St. Lawrence, Canada. Climate Dynamics 46 (1), 449–466.

Scott, K. A., Ashouri, Z., Buehner, M., Pogson, L., Carrieres, T., 2015. Assimilation of ice and water observations from SAR imagery to improve estimates of sea ice concentration. Tellus A : Dynamic Meteorology and Oceanography 67 (1), 27218.

Smith, G. C., Roy, F., Brasnett, B., 2013. Evaluation of an operational ice – ocean analysis and forecasting system for the Gulf of St Lawrence. Royal Meteorological Society 139 (January 2013 B), 419–433.

Soh, L.-k., Tsatsoulis, C., 1999. Texture Analysis of SAR Sea Ice Imagery Using Gray Level Co-Occurrence Matrices. IEEE Transactions on Geoscience and Remote Sensing 37 (2), 780 – 795.

Squire, V. A., Moore, S. C., 1980. Direct measurement of the attenuation of ocean waves by pack ice. Nature 283 (5745), 365–368.

Sutherland, G., Rabault, J., Christensen, K. H., Jensen, A., 2018. A two layer model for wave dissipation in sea ice. arXiv :1805.01134 [physics.ao-ph], 15p.

Wadhams, P., Squire, V. A., Goodman, D. J., Cowan, A. M., Moore, S. C., 1988. The attenuation rates of ocean waves in the marginal ice zone. Journal of Geophysical Research : Oceans 93 (C6), 6799–6818.

Williams, T. D., Bennetts, L. G., Squire, V. A., Dumont, D., Bertino, L., 2013. Wave – ice interactions in the marginal ice zone . Part 1 : Theoretical foundations. Ocean Modelling 71, 81–91.

CONCLUSION GÉNÉRALE

Les efforts déployés au cours de la présente étude ont permis le développement d'une version de WIM, laquelle inclut les échanges non linéaires d'énergie entre les vagues. Dans le contexte hivernal de l'estuaire du Saint-Laurent où la couverture de glace est partielle et variable, et considérant l'importance des échanges énergétiques vagues-vagues pour la migration de la période modale vers les basses fréquences, cette implémentation a permis d'étendre la zone de modélisation au-delà d'une région complètement recouverte de glace. Forcé par le vent, un spectre de vague croît ainsi suivant une grille spatiale 1-D caractérisée par l'épaisseur et la concentration de glace associée.

Dans un premier temps, et en absence de données in situ pour ce faire, la calibration du modèle WIM avec les modèles WW3 et GENER a permis de quantifier la progression en eaux libres du spectre de vagues se propageant dans une direction. Dans un deuxième temps, des grilles spatiales 1-D extraites d'images SAR pour l'estuaire du Saint-Laurent furent soumises à WIM et une analyse qualitative et quantitative des résultats a permis de faire ressortir certaines questions fondamentales. La comparaison avec les données de vagues des AWAC pour les 3 cas d'études identifiés ont toutefois mis en évidence une large différence entre les données in situ et les sorties de modèle.

Il importe de préciser que WIM est un modèle jouet. En ce sens, il ne vise pas à reproduire avec exactitude le résultat d'un modèle de plus grande complexité ou encore les observations in situ, mais doit néanmoins pouvoir représenter de manière réaliste le comportement de spectres de vague. Le faible échantillonnage de données de vagues fourni par les AWAC mouillés au Bic et à Forestville rend cependant difficile de conclure à l'incompatibilité du modèle avec l'objectif visé. Ce constat met néanmoins en lumière la forte dépendance entre le succès d'une telle approche et la double disponibilité des images SAR pour la glace et celle des données in situ pour les vagues.

Résultats clés

Alors que l'objectif initial reposait à la fois sur une meilleure compréhension des interactions vagues-glace, mais aussi sur la composante méthodologique du projet, le traitement des données a permis de mettre en lumière certains résultats :

1. Les interactions non linéaires entre les vagues contribuent fortement à la migration de la période modale vers les basses fréquences. Dans un contexte où le taux d'atténuation des vagues par la glace est fonction de la fréquence, un tel mécanisme apparaît incontournable pour représenter l'évolution du spectre de vague dans des régions où, localement, la glace est partielle ou discontinuement distribuée.
2. L'imagerie SAR offre un accès à une large source de données pertinentes pour caractériser la distribution de glace de mer. Cependant, dans la perspective d'étudier les interactions vagues-glace, de nombreuses images furent rejetées. Conséquemment, l'approche repose largement sur l'accès à un grand nombre d'images pour maximiser la probabilité d'y retrouver à la fois une distribution de glace partielle et discontinue, la présence de vagues pour la période et la disponibilité de données in situ pour la mesure de celles-ci.

Potentiel d'application future

La prémisse sous-tendant WIM suppose qu'il est possible de représenter l'évolution d'un spectre de vague au moyen d'une grille spatiale 1D. De plus, la grande complexité à regrouper l'ensemble des données nécessaires à l'étude de l'interaction vagues-glace rend la validation même de cette hypothèse ardue et les résultats qui en découlent d'autant plus sensibles. L'intérêt d'un modèle comme WIM réside donc dans sa simplicité d'utilisation et sa rapidité en temps de calcul. Or, avec l'implémentation des interactions vagues-vagues, le niveau de complexité du modèle augmente inversement à la pertinence de son utilisation.

En effet, de nombreux modèles 2-D actuellement en opération pour la prévision ou la recherche proposent de nombreuses paramétrisations de glace. C'est le cas de WW3 ou de SWAN, par exemple. En absence d'une plus grande source de données, l'intégration de la méthodologie actuelle à un tel modèle déjà existant et dont l'utilisation est davantage répandue semble représenter un meilleur investissement pour une phase ultérieure.

RÉFÉRENCES

Ardhuin, F., Boutin, G., Stopa, J., Girard-Ardhuin, F., Melsheimer, C., Thomson, J., Kohout, A., Doble, M., Wadhams, P., 2018. Wave Attenuation Through an Arctic Marginal Ice Zone on 12 October 2015 : 2 . Numerical Modeling of Waves and Associated Ice Breakup. Journal of Geophysical Research : Oceans 123 (8), 5652–5668.

Bismuth, E., 2014. Interactions vagues-glace dans l'estuaire et le golfe du Saint-Laurent. Mémoire de maîtrise, Université du Québec à Rimouski, 96 p.

Booij, N., Haagsma, I., Holthuijsen, L., Kieftenburg, A., Ris, R., van der Westhuysen, A., Zijlema, M., 2006. SWAN Technical Documentation. Delft University of Technology. The Netherlands.

Booij, N., Ris, R. C., Holthuijsen, L. H., 1999. A third-generation wave model for coastal regions 1 . Model description and validation. Journal of Geophysical Research 104 (C4), 7649–7666.

Cavaleri, L., Alves, J.-H., Ardhuin, F., Babanin, A., Banner, M., Belibassakis, K., Benoit, M., Donelan, M., Groeneweg, J., Herbers, T. H. C., Hwang, P., Janssen, P. A. E. M., Janssen, T., Lavrenov, I. V., Magne, R., Monbalui, J., Onorato, M., Polnikov, V., Resio, D., Rogers, W., Sheremet, A., McKee Smith, J., Tolman, H., van Vledder, G., Wolf, J., Young, I., 2007. Wave modelling – The state of the art. Progress in Oceanography 75, 603–674.

Cavaleri, L., Rizzoli, P. M., 1981. Wind wave prediction in shallow water: Theory and applications. Journal of Geophysical Research: Oceans 86 (C11), 10961–10973.

Cheng, S., Rogers, W. E., Thomson, J., Smith, M., Doble, M. J., Persson, O. P. G., Iii, C. O. C., Wadhams, P., Kohout, A. L., Ackley, S. F., Montiel, F., Shen, H. H., 2017. Calibrating a Viscoelastic Sea Ice Model for Wave Propagation in the Arctic Fall Marginal Ice Zone. Journal of Geophysical Research : Oceans 122, 8770–8793.

Clausi, D. A., 2001. Comparison and fusion of co-occurrence , Gabor and MRF texture features for classification of SAR sea-ice imagery. Atmosphere-Ocean 39 (3), 183–194.

Collins, C. O., Rogers, W. E., Marchenko, A., Babanin, A. V., 2015. In situ measurements of an energetic wave event in the Arctic marginal ice zone. Geophysical Research Letters 42, 1863–1870.

Doble, M. J., De Carolis, G., Meylan, M. H., Bidlot, J.-R., Wadhams, P., 2015. Relating wave attenuation to pancake ice thickness, using field measurements and model results. Geophysical Research Letters 42, 4473–4481.

Dumont, D., Baudry, J., Sutherland, P., Barst, L., 2020. Constraining wave dissipation and non-linear interactions in the marginal ice zone Poster session presented at : Ocean Sciences Meeting, 16-21 February, San Diego, USA.

Dumont, D., Kohout, A., Bertino, L., 2011. A wave based model for the marginal ice zone including a floe breaking parameterization. Journal of Geophysical Research 116 (C04001), 1–12.

Goda, Y., 1988. Statistical variability of sea state parameters as a function of wave spectrum. Coastal Engineering in Japan 31 (1), 39–52.

Goda, Y., 1999. A Comparative Review on the Functional Forms of Directional Wave Spectrum. Coastal Engineering Journal 41 (1), 1–20.

Goda, Y., Suzuki, Y., 1975. Computation of refraction and diffraction of sea waves with Mitsuyasu's directional spectrum. Technical Note, Port and Harbour Research Institue 230, 45 p.

Hasselmann, D., Bösenberg, J., 1991. Field measurements of wave-induced pressure over wind-sea and swell. Journal of Fluid Mechanics 230, 391–428.

Hasselmann, K., 1962. On the non-linear energy transfer in a gravity-wave spectrum part 1. general theory. Journal of Fluid Mechanics 12 (4), 481–500.

Hasselmann, K., 1974. On the spectral dissipation of ocean waves due to white capping. Boundary - Layer Meteorology 6, 107–127.

Hasselmann, K., Barnett, T. P., Bouws, E., Carlson, H., Cartwright, D. E., Enke, K., Ewing, J. A., Gienapp, H., Hasselmann, D. E., Kruseman, P., Meerburg, A., Müller, P., Olbers, D. J., Richter, K., Sell, W., Walder, H., 1973. Measurements of Wind-Wave Growth and Swell Decay during the Joint North Sea Wave Project (JONSWAP).

Hasselmann, S., Hasselmann, K., 1985. Computations and Parameterizations of the Nonlinear Energy Transfer in a Gravity-Wave Spectrum. Part I : A New Method for Efficient Computations of the Exact Nonlinear Transfer Integral. Journal of Physical Oceanography 15 (11), 1369–1377.

Hasselmann, S., Hasselmann, K., Allender, J. H., Barnett, T. P., 1985. Computations and Parameterizations of the Nonlinear Energy Transfer in a Gravity-Wave Specturm. Part II : Parameterizations of the Nonlinear Energy Transfer for Application in Wave Models. Journal of Physical Oceanography 15 (11), 1378–1391.

Holland, M. M., Stroeve, J., 2011. Changing seasonal sea ice predictor relationships in a changing Arctic climate. Geophysical Research Letters 38 (L18501), 1–6.

Holthuijsen, L. H., 2007. Waves in Oceanic and Coastal Waters. Cambridge University Press, Campbridge.

J Saucier, F., Roy, F., Gilbert, D., Pellerin, P., Ritchie, H., 2003. Modeling the formation and circulation processes of water masses and sea ice in the Gulf of St . Lawrence , Canada. Journal of Geophysical Research 108 (C8), 1–20.

Komen, G. J., Hasselmann, S., Hasselmann, K., 1984. On the Existence of a Fully Developed Wind-Sea Spectrum. American Meteorological Society 14, 1271–1295.

Lee, J. S., Jurkevich, L., Dewaele, P., Wambacq, P., Oosterlinck, A., 1994. Speckle filtering of synthetic aperture radar images : A review. Remote Sensing Reviews 8 (4), 313–340.

Li, J., Kohout, A. L., Doble, M. J., Shen, H. H., Wadhams, P., Guan, C., 2017. Rollover of Apparent Wave Attenuation in Ice Covered Seas. Journal of Geophysical Research : Oceans 122, 8557–8566.

Liu, A. K., Holt, B., Vachon, P. W., 1991. Wave propagation in the marginal ice zone: Model predictions and comparisons with buoy and synthetic aperture radar data. Journal of Geophysical Research : Oceans 96 (C3), 4605–4621.

Mason, L. A., Riseng, C. M., Layman, A. J., Jensen, R., 2018. Effective fetch and relative exposure index maps for the Laurentian Great Lakes. Sci Data 5 (180295), 1–7.

Masson, D., Leblond, P. H., 1989. Spectral evolution of wind-generated surface gravity waves in a dispersed ice field. Journal of Fluid Mechanics 202, 43–81.

Meylan, M. H., Bennetts, L. G., Kohout, A. L., 2014. In situ measurements and analysis of ocean waves in the Antarctic marginal ice zone. Geophysical Research Letters 41, 5046–5051.

Miles, J. W., 1957. On the generation of surface waves by shear flows. Journal of Fluid Mechanics 3 (2), 185–204.

Mitsuyasu, H., Tasai, F., Suhara, T., Mizuno, S., Ohkusu, M., Honda, T., Rikiishi, K., 1975. Observations of the Directional Spectrum of Ocean Waves Using a Cloverleaf Buoy 5, 750–760.

Montiel, F., Squire, V. A., Bennetts, L. G., 2016. Attenuation and directional spreading of ocean wave spectra in the marginal ice zone. Journal of fluid mechanics 790, 492–522.

Moreira, A., Prats-iraola, P., Younis, M., Krieger, G., Hajnsek, I., Papathanassiou, K. P., 2013. A Tutorial on Synthetic Aperture Radar. IEEE Geoscience and Remote Sensing Magazine (march), 6–43.

Mosig, J. E. M., Montiel, F., Squire, V. A., 2015. Comparison of viscoelastic-type models for ocean wave attenuation in ice-covered seas. Journal of Geophysical Research : Oceans 120, 6072–6090.

Neumeier, U., Ruest, B., Lambert, A., Bismuth, E., Dumont, D., Jacob, D., Savard, J.-P., Joly, S., 2013. Modélisation du régime des vagues du golfe et de l'estuaire du Saint-Laurent pour l'adaptation des infrastructures côtières aux changements climatiques (rapport final présenté au ministère des Transports du Québec). Tech. rep.

Ochilov, S., Clausi, D. A., 2010. Automated Classification of Operational SAR Sea Ice Images. In: Canadian Conference Computer and Robot Vision. Waterloo, ON, Canada, pp. 40–46.

Ochilov, S., Clausi, D. A., 2012. Operational SAR Sea-Ice Image Classification. IEEE Transactions on Geoscience and Remote Sensing 50 (11), 4397 – 4408.

Phillips, O. M., 1957. On the generation of waves by turbulent wind. Journal of Fluid Mechanics 2 (5), 417–445.

Resio, D. T., Perrie, W., 2008. A two-scale approximation for efficient representation of nonlinear energy transfers in a wind wave spectrum. Journal of Physical Oceanography 38, 1–37.

Ruest, B., Neumeier, U., Dumont, D., Bismuth, E., Senneville, S., Caveen, J., 2016. Recent wave climate and expected future changes in the seasonally ice-infested waters of the Gulf of St. Lawrence, Canada. Climate Dynamics 46 (1), 449–466.

Scott, K. A., Ashouri, Z., Buehner, M., Pogson, L., Carrieres, T., 2015. Assimilation of ice and water observations from SAR imagery to improve estimates of sea ice concentration. Tellus A : Dynamic Meteorology and Oceanography 67 (1), 27218.

Smith, G. C., Roy, F., Brasnett, B., 2013. Evaluation of an operational ice – ocean analysis and forecasting system for the Gulf of St Lawrence. Royal Meteorological Society 139 (January 2013 B), 419–433.

Snyder, R. L., Dobson, F. W., Elliott, J. A., Long, R. B., 1981. Array measurements of atmospheric pressure fluctuations above surface gravity waves. Journal of Fluid Mechanics 102, 1–59.

Soh, L.-k., Tsatsoulis, C., 1999. Texture Analysis of SAR Sea Ice Imagery Using Gray Level Co-Occurrence Matrices. IEEE Transactions on Geoscience and Remote Sensing 37 (2), 780 – 795.

Squire, V. A., Moore, S. C., 1980. Direct measurement of the attenuation of ocean waves by pack ice. Nature 283 (5745), 365–368.

Stephenson, S. R., Smith, L. C., Agnew, J. A., 2011. Divergent long-term trajectories of human access to the Arctic. Nature Climate Change 1 (5), 1–5.

Stroeve, J., Hamilton, L. C., Bitz, C. M., Blanchard-wrigglesworth, E., 2014. Predicting September sea ice : Ensemble skill of the SEARCH Sea Ice Outlook 2008-2013. Geophysical Research Letters 41 (7), 2411–2418.

Sutherland, G., Rabault, J., Christensen, K. H., Jensen, A., 2018. A two layer model for wave dissipation in sea ice. arXiv:1805.01134 [physics.ao-ph], 15p.

Sutherland, G., Rabault, J., Christensen, K. H., Jensen, A., 2019. A two layer model for wave dissipation in sea ice. Applied Ocean Research 88 (March), 111–118. URL https://doi.org/10.1016/j.apor.2019.03.023

Tang, C. L., Yao, T., Perrie, W., B M, D., Toulany, B., Dunlap, E., Wu, Y., 2008. BIO Ice-Ocean and Wave Forecasting Models and Systems for Eastern Canadian Waters. Tech. Rep. 261.

The WAMDI group, 1988. The WAM Model - A Third Generation Ocean Wave Prediction Model. American Meteorological Society 18, 1775–1810.

Thomson, J., Rogers, W. E., 2014. Swell and sea in the emerging Arctic Ocean. Geophysical Research Letters 41, 3136–3140.

Tolman, H. L., 1991. A Third-Generation Model for Wind Waves on Slowly Varying Unsteady, and Inhomogeneous Depths and Currents. Journal of Physical Oceanography 21, 782–797.

Tolman, H. L., 1992. Effects of numerics on the physics in a third-generation wind-wave model. Journal of Physical Oceanography 22 (10), 1095–1111.

Tolman, H. L., 2009. User manual and system documentation of WAVEWATCH-IIITM version 3.14. User manual and system documentation of WAVEWATCH III version 3.14 (3.14), 220.

Tolman, H. L., Banner, M. L., Kaihatu, J. M., 2013. The NOPP operational wave model improvement project. Ocean Modelling 70, 2–10.

Tolman, H. L., Krasnopolsky, V. M., 2004. Nonlinear interactions in practical wind wave models. In: 8Th International Workshop on Wave Hindcasting and Forecasting. Maryland, USA, p. 15 p.

Tuomi, L., Kahma, K. K., Pettersson, H., 2011. Wave hindcast statistics in the seasonally ice-covered Baltic Sea 16 (December), 451–472.

van Vledder, G. P., 2006. The WRT method for the computation of non-linear four-wave interactions in discrete spectral wave models. Coastal Engineering 53 (2-3), 223–242.

van Vledder, G. P., 2012. Efficient algorithms for non-linear four-wave interactions. In: ECMWF workshop on Ocean Waves. Reading (England), pp. 97–112.

Wadhams, P., 1978. Wave decay in the marginal ice zone measured from a submarine. Deep-Sea Res 25, 23–40.

Wadhams, P., Squire, V. A., Goodman, D. J., Cowan, A. M., Moore, S. C., 1988. The attenuation rates of ocean waves in the marginal ice zone. Journal of Geophysical Research: Oceans 93 (C6), 6799–6818.

Williams, T. D., Bennetts, L. G., Squire, V. A., Dumont, D., Bertino, L., 2013a. Wave – ice interactions in the marginal ice zone . Part 1 : Theoretical foundations. Ocean Modelling 71, 81–91.

Williams, T. D., Bennetts, L. G., Squire, V. A., Dumont, D., Bertino, L., 2013b. Wave – ice interactions in the marginal ice zone . Part 2 : Numerical implementation and sensitivity studies along 1D transects of the ocean surface. Ocean Modelling 71, 92–101.

WMO, 1998. Guide to Wave Analysis and Forecasting. World Meteorological Organization.

Wu, J., 1982. Wind-stress coefficients over sea surface from breeze to hurricane. Journal of Geophysical Research: Oceans 87 (C12), 9704–9706.

Wyatt, L. R., Green, J. J., Middleditch, A., 2011. HF radar data quality requirements for wave measurement. Coastal Engineering 58 (4), 327–336.

Young, I. R., Babanin, A. V., 2006. Spectral Distribution of Energy Dissipation of Wind-Generated Waves due to Dominant Wave Breaking. Journal of Physical Oceanography 36, 376–394.

Young;, I. R., van Vledder, G. P., 1993. A Review of the Central Role of Nonlinear Interactions in Wind-Wave Evolution. The Royal Society publishing 342 (1666), 505–524.

ANNEXE A

SENTINEL-1A METADATA

Table 4: Metadata for all SAR images used as ROI.

	SAR 1	SAR 2	SAR 3
Date	2017-01-09	2018-01-04	2018-01-28
Proc time (UTC)	22h28	22h28	22h28
Mission ID	Sentinel-1A	Sentinel-1A	Sentinel-1A
Product type	GRD	GRD	GRD
Aquisition Mode	IW	IW	IW
Polarisation	VV	VV	VV
Radar frequency (MHz)	5.405	5.405	5.405
Spatial resolution	10 m	10 m	10 m
Pass	Ascending	Ascending	Ascending
Antenna pointing	Right	Right	Right
Incidence (near)	30.5	30.5	30.5
Incidence angle (far)	45.9	45.9	45.9

ANNEXE B

LIST OF IMAGES

TABLE 5: Images from SENTINEL-1

Date	Type	Wind	Dir	< C >	AWAC
20150316	S1	3	ENE	50	AAL
20150321	S1	2	SE	10	AAL
20170104	S1	3	E	0	F, B
20170109	S1	12	SSE	15	F, B
20170121	S1	3	W	15	F, B
20170214	S1	5	ENE	60	F, B
20170221	S1	4	E	*	F, B
20170305	S1	8	NW	50	F, B
20170317	S1	2	**	*	F, B
20170329	S1	*	**	0	F, B
20171218	S1	7	SW	20	F, B
20171223	S1	8	E	75	F, B
20171230	S1	6	W	90	F, B
20180104	S1	11	ENE	80	B
20180111	S1	11	SSW	20	B
20180116	S1	9	NW	*	B
20180128	S1	6	WNW	20	B
20180209	S1	4	SW	100	B
20180216	S1	8	NW	*	B
20180221	S1	11	NW	0	B
20180228	S1	12	NE	10	B
20180305	S1	10	NE	15	B
20180312	S1	7	ENE	20	B

Table 6: Images from RADARSAT-2

Date	Type	Wind	Dir	< C >	AWAC
20140116	RS2	5	NE	10	-
20140117	RS2	5	ENE	15	-
20140123	RS2	8	NW	90	-
20140124	RS2	7	NW	90	-
20140127	RS2	5	SE	20	-
20140209	RS2	4	W	*	-

Table 7: Images from MODIS

Date	Type	Wind	Dir	< C >	AWAC
20160125	MOD	2	**	50	F, B
20160130	MOD	3	SSW	20	F, B
20160222	MOD	8	WNW	30	F, B
20160320	MOD	5	S	40	F, B
20170123	MOD	3	NE	*	F, B
20170207	MOD	2	N	10	F, B
20170209	MOD	3	SW	50	F, B
20170220	MOD	6	NNE	50	F, B
20170221	MOD	1	SE	50	F, B
20170228	MOD	6	SW	5	F, B
20170304	MOD	10	NW	50	F, B
20170305	MOD	8	NW	50	F, B
20170306	MOD	2	NNW	80	F, B
20170318	MOD	4	WSW	60	F, B
20170319	MOD	2	SW	20	F, B
20170323	MOD	10	NW	30	F, B
20170325	MOD	9	NW	5	F, B
20180121	MOD	7	WNW	*	B
20180122	MOD	5	NW	*	B
20180204	MOD	9	NE	100	B
20180213	MOD	8	SW	*	B
20180217	MOD	7	NW	*	B
20180217	MOD	6	W	*	B
20180221	MOD	8	W	0	B

ANNEXE C

CIS ICE CHARTS CORRESPONDING TO STUDY CASES

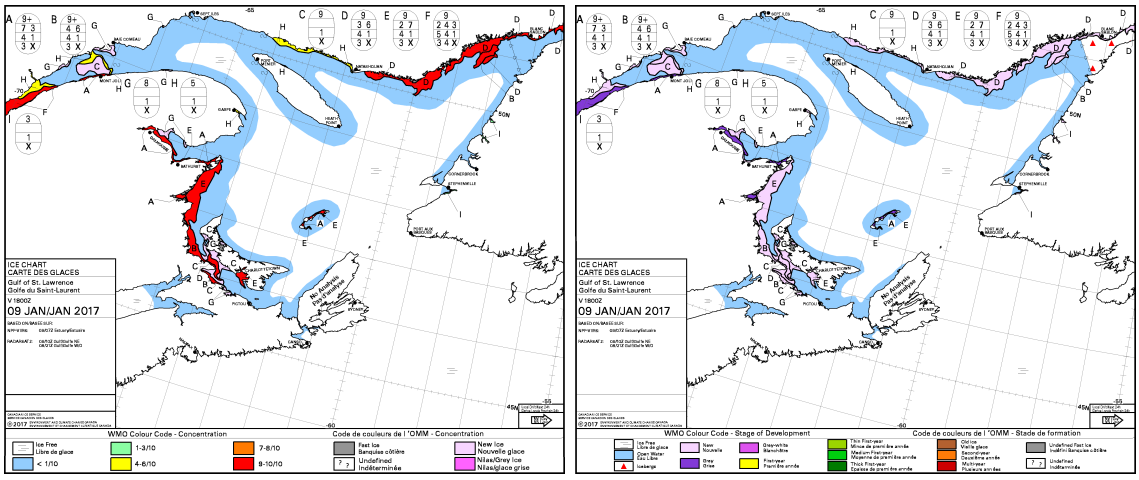

FIGURE 28: CIS ice charts for SC1.

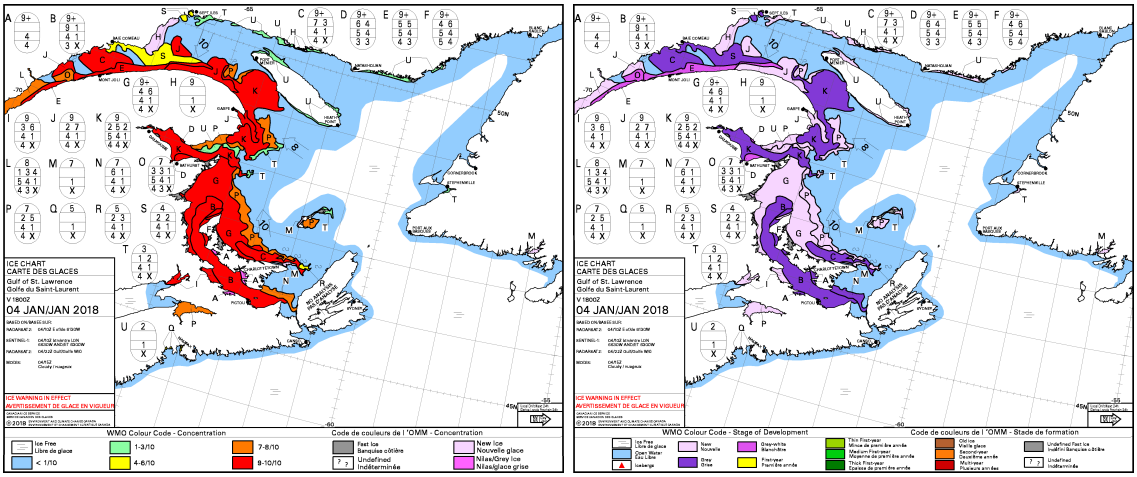

FIGURE 29: CIS ice charts for SC2.

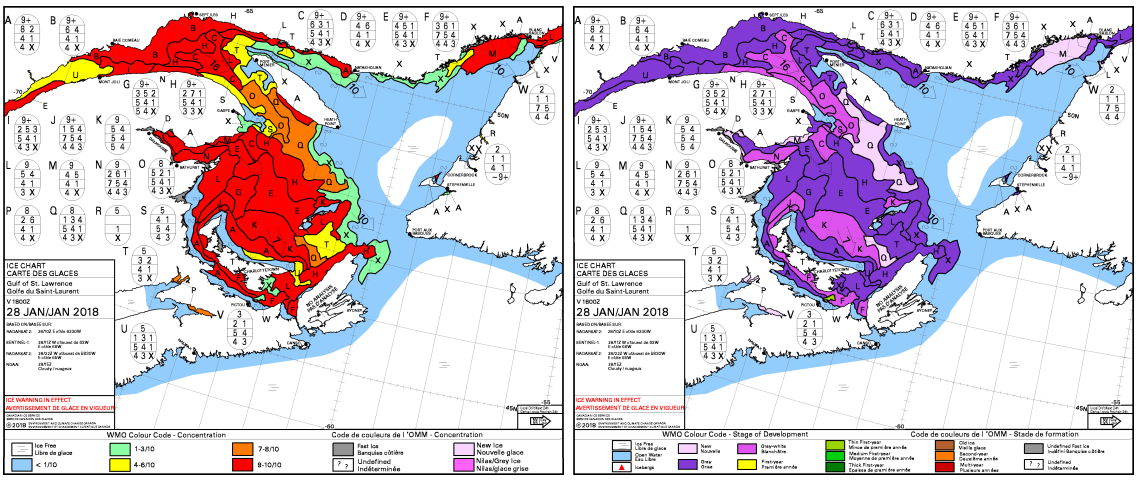

FIGURE 30: CIS ice charts for SC3.